RSC Advances

PAPER

View Article Online
View Journal | View Issue

Cite this: *RSC Adv.*, 2025, **15**, 8809

Synthesis, radiolabeling, and biological evaluation of methyl 6-deoxy-6-[^{18}F]fluoro-4-thio-α-D-maltotrioside as a positron emission tomography bacterial imaging agent†

Kiyoko Takemiya, *[a] Wonewoo Seo,[bc] Ronald J. Voll,[bc] Sheng Zhao,[d] Giji Joseph,[a] Shelly Wang,[a] Fanxing Zeng,[bc] Jonathon A. Nye,[bce] Niren Murthy,[d] W. Robert Taylor[afg] and Mark M. Goodman‡[bc]

We developed fluorine-18 ([^{18}F]) labeled methyl 6-deoxy-6-fluoro-4-thio-α-D-maltotrioside ([^{18}F]MFTMT) for bacterial imaging and evaluated its stability and efficacy *in vitro* and *in vivo*. We found that *Staphylococcus aureus* (*S. aureus*) internalized [^{18}F]MFTMT whereas *Escherichia coli* (*E. coli*) and CHO-K1 cells did not, in *in vitro*. Positron emission tomography imaging with [^{18}F]MFTMT revealed that radioactivity accumulated not only in the *S. aureus*-infected group but also in the *E. coli*-infected and non-infectious inflammation groups. Further studies revealed that rat serum digested [^{18}F]MFTMT into [^{18}F]-methyl 6-deoxy-6-fluoro-4-thio-α-D-maltoside ([^{18}F]MFTM), while [^{18}F]MFTMT was stable in human serum for 210 min. [^{18}F]MFTM was identified as the only radioactive metabolite *in vivo*. Similar to [^{18}F]MFTMT, [^{18}F]MFTM was internalized only by *S. aureus*. [^{18}F]MFTM was identified as the only radioactive metabolite *in vivo*. We found that the sodium–glucose co-transporter 1 (SGLT1) is expressed in inflammatory tissue, and SGLT1 overexpressing cells showed increased retention of [^{18}F]MFTMT and [^{18}F]MFTM *in vitro*. Our study showed that the thio-glycosyl bond is stable against enzymatic digestion, and maltotetraose or a longer maltodextrin backbone is desirable for bacteria-specific imaging to avoid nonspecific uptake by SGLT1.

Received 29th January 2025
Accepted 11th March 2025

DOI: 10.1039/d5ra00693g

rsc.li/rsc-advances

Introduction

Bacterial infections pose formidable health challenges, often leading to severe tissue damage and necessitating major surgical interventions.[1–7] Diseases such as endocarditis and infections associated with medical devices are particularly concerning, underscoring the critical need for accurately localizing bacteria within target organs or tissues to facilitate their diagnosis and treatment.[6,8–14] Early detection of bacterial infections using non-invasive methods could enable the timely administration of antibiotic therapy, potentially preventing tissue damage and reducing treatment costs.

Currently, no established non-invasive diagnostic methods specifically detect the existence of bacteria in deep organs and/or tissue directly. Non-invasive diagnostic methods, such as computed tomography (CT) and ultrasound, detect the tissue damage induced by bacterial infection, and contrast CT and 2-deoxy-2-[^{18}F]fluoro-D-glucose ([^{18}F]FDG) positron emission tomography (PET) imaging detect the increase of blood flow and glucose uptake induced by inflammation.[15] However, there can be false positive results from these tests because of sterile inflammation. Thus, for the specific detection of bacterial infection, new methods to detect the existence of bacteria are required.

[a]*Division of Cardiology, Department of Medicine, Emory University School of Medicine, 1750 Haygood Dr NE, Atlanta, Georgia, 30322, USA. E-mail: kiyoko.takemiya@emory.edu*

[b]*Department of Radiology and Imaging Sciences, School of Medicine, Emory University, 1841 Clifton Road NE, Atlanta, Georgia, 30322, USA*

[c]*Center for Systems Imaging, Emory University, 1364 Clifton Rd NE, Atlanta, Georgia, 30022, USA*

[d]*Department of Bioengineering, University of California at Berkeley, Stanley Hall 306, Berkeley, California, 94720, USA*

[e]*Department of Radiology and Radiological Science, Medical University of South Carolina, 261 Calhoun Street, Charleston, South Carolina, 29425, USA*

[f]*Joseph Maxwell Cleland Atlanta VA Medical Center, 1670 Clairmont Road, Decatur, Georgia, 30033, USA*

[g]*Wallace H. Coulter Department of Biomedical Engineering, School of Medicine, Emory University, 1750 Haygood Dr NE, Atlanta, Georgia, 30322, USA*

† Electronic supplementary information (ESI) available: ^{1}H, ^{13}C, and ^{19}F NMR spectra for MFTMT (**6**) and MFTM (**13**), radiometric HPLC data for [^{18}F]**13**, timelines of biological experiments, radiometric HPLC data for enzymatically digested [^{18}F]MFTMT, body weights of animals, intensity of injected radioactivity for PET imaging, the numeric values of bacteria/cell uptake studies and PET imaging analysis data, and molecular formula strings. See DOI: https://doi.org/10.1039/d5ra00693g

‡ Co-corresponding author.

We have been focusing on the differences in sugar metabolism between bacteria and mammalian cells. Bacteria utilize maltose and maltodextrins *via* the maltodextrin transporter and phosphotransferase system (PTS) as both are specific and ubiquitous expressed in bacteria. Mammalian cells do not have maltodextrin transporter nor PTS, and they do not internalize maltose and maltodextrins. Comparing the maltodextrin transporter and PTS, the maltodextrin transporter has tremendous potential for *in vivo* bacterial imaging[16–19] because of its specific expression in bacteria and presence in both Gram-positive and Gram-negative bacteria and because of its capacity to transport a molecule conjugated to maltodextrin.[20–24] The maltodextrin transporter actively transports maltodextrins up to maltoheptaose and can recognize imaging molecules conjugated to the maltodextrin backbone.[16–23,25] Several studies have validated the efficacy of maltodextrin-based imaging probes in targeting the maltodextrin transporter and visualizing bacteria *in vivo*.[16–19,25–27] For example, probes incorporating a maltohexaose backbone conjugated with imaging molecules at the anomeric carbon demonstrated high sensitivity and specificity in both *in vitro* and *in vivo* bacterial imaging scenarios.[16–19]

Among many imaging modalities, such as PET, CT and magnetic resonance imaging (MRI), the radioactive tracers are known to be more sensitive than other modalities.[28–30] Fluorine-18 ([^{18}F]) can replace the hydroxyl group by derivatization of maltodextrins or can be conjugated with a linker molecule.[17,18,31] We have shown that [^{18}F] conjugated maltohexaose ([^{18}F]MHF) accumulates only in bacterial infection lesions and does not accumulate in non-infectious inflammation lesions.[17,18] In contrast, [^{18}F]FDG accumulates in both bacterial infection lesion and non-infectious inflammation lesion.[18] Our previous studies demonstrated the potential of maltohexaose-based imaging probes for the specific detection of bacterial infections.[17–19]

One limitation of the maltohexaose backbone lies in its susceptibility to degradation *via* serum amylases and α-glucosidases, generating various sugars that may be internalized by mammalian cells, causing nonspecific uptake of labeled metabolites, such as glucose and maltose.[32–36]

To enhance the stability of the maltodextrin backbone, we propose incorporating a thio-glycosyl bond to confer resistance against enzymatic digestion to improve stability of the maltodextrin backbone. This study focused on the development of fluorine-18 labeled methyl 6-deoxy-6-fluoro-4-thio-α-D-maltotrioside ([^{18}F]MFTMT) and assessed its serum stability. Additionally, we investigated the uptake of [^{18}F]MFTMT by bacteria *in vitro* and assessed its efficacy in detecting bacterial infections *in vivo* using a device infection model.

Results

Chemistry

The synthesis of the cold standard methyl 6-deoxy-6-fluoro-4-thio-α-D-maltotrioside (**6**) and the synthesis of the [^{18}F]-labeling precursor methyl 6-(4-bromobenzenesulfonyloxy(brosyloxy))-4-thio-α-D-maltotrioside (**10**) is described in Schemes 1 and 2,

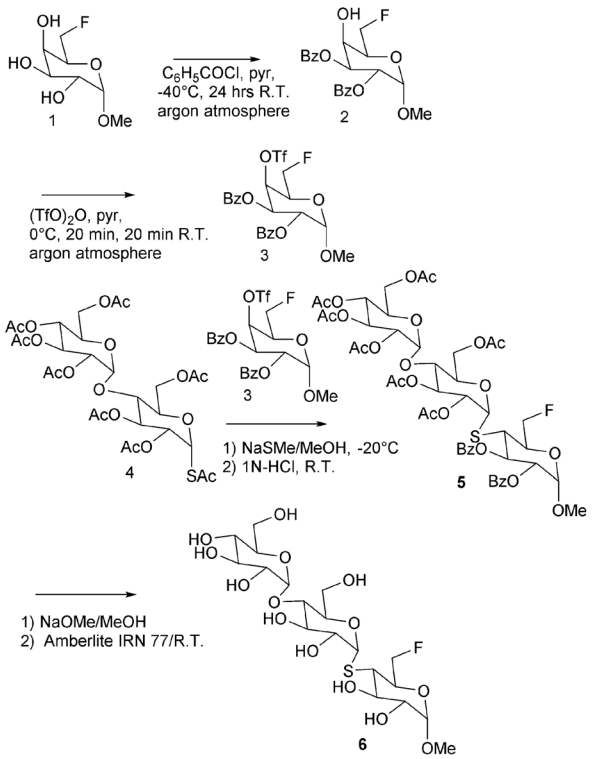

Scheme 1 Synthesis of methyl 6-deoxy-6-fluoro-4-thio-α-D-maltotrioside cold standard (**6**).

respectively. The main advantage for the 4-bromobenzenesulfonyloxy ester is that nucleophilic substitution proceeds more efficiently compared to the use of the corresponding 4-methylbenzenesulfonyloxy ester.[37]

Methyl 6-deoxy-6-fluoro-4-thio-α-D-maltotrioside **6** (MFTMT) was synthesized in a four-step reaction sequence starting from methyl 6-deoxy-6-fluoro-α-D-galactopyranose[38] **1** (Scheme 1). Reaction of **1** with benzoyl chloride in pyridine afforded the 2,3-dibenzoyl compound **2**. Treatment of **2** with triflic anhydride in pyridine gave the triflate **3**. Reaction of **3** with 2,3,6-tri-*O*-acetyl-*S*-acetyl-(2,3,4,6-tetra-*O*-acetyl-*S*-acetyl-1-thio-α-D-glucopyranosyl)-α-D-glucopyranose[39] **4** according to the literature procedure[40] afforded 4-thio-maltotrioside **5**. Removal of the acetate and benzoate groups by treatment with $NaOCH_3$–CH_3OH gave **6** followed by purification on silica resulting in a 51% yield. Compound **6** was prepared in 9% overall yield from compound **1**.

We employed a similar route to synthesize the [^{18}F]-labeling precursor methyl 6-brosyloxy-4-thio-α-D-maltotrioside **10** (Scheme 2). Methyl 2,3-di-*O*-benzoyl-4-trifluoromethylsulfonyl-6-*O*-trityl-α-D-galactopyranoside[41] **7** was treated with 2,3,6-tri-*O*-acetyl-*S*-acetyl-(2,3,4,6-tetra-*O*-acetyl-*S*-acetyl-1-thio-α-D-glucopyranosyl)-α-D-glucopyranose to afford the trityl ether **8**. A sequential reaction of **8** with aqueous acetic acid and brosyl chloride afforded the C-6 brosyloxy precursor **10** resulting in a 65% yield.

We next turned our attention to the synthesis of methyl 6-deoxy-6-fluoro-4-thio-α-D-maltoside. It was anticipated that this compound may be the product of rat serum α-glucosidase metabolism of methyl 6-deoxy-6-fluoro-4-thio-α-D-maltotrioside.

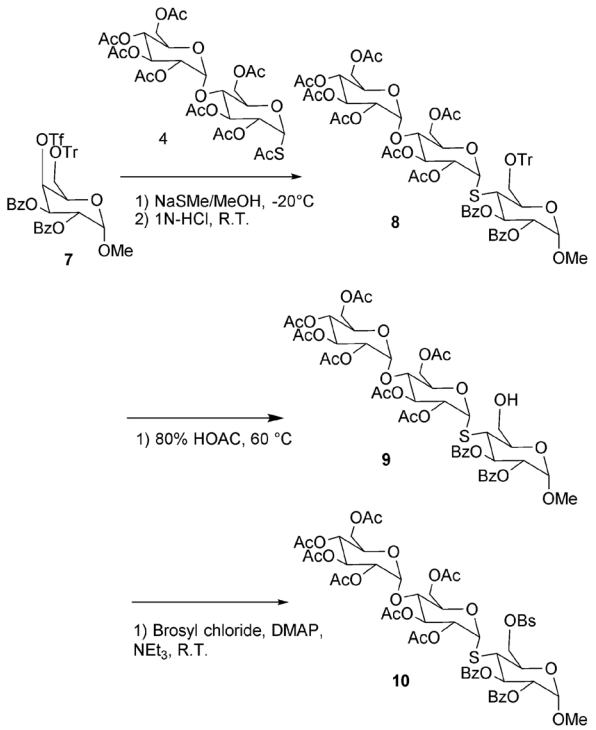

Scheme 2 Synthesis of methyl 6-brosyloxy-4-thio-α-D-maltotrioside [^{18}F] labeling precursor (**10**).

Methyl 6-deoxy-6-fluoro-4-thio-α-D-maltoside **13** was synthesized in a two-step reaction sequence starting from methyl 2,3-di-*O*-benzoyl-4-*O*-trifluoromethylsulfonyl-6-deoxy-6-fluoro-α-D-galactopyranoside **3** (Scheme 3). Reaction of **3** with 2,3,4,6-tetra-*O*-acetyl-*S*-acetyl-1-thio-α-D-glucopyranose[42] **11** according to the literature procedure[40] afforded 4-thio-maltoside **12** in 59% yield. Removal of the acetate and benzoate groups by treatment with $NaOCH_3$–CH_3OH gave **13** following purification on silica with a 99% yield.

Radiochemistry

The automated synthesis of [^{18}F]MFTMT ([^{18}F]**6**) (Scheme 4) was carried out in a cGMP compliant device, the GE TracerLab FX 2N.

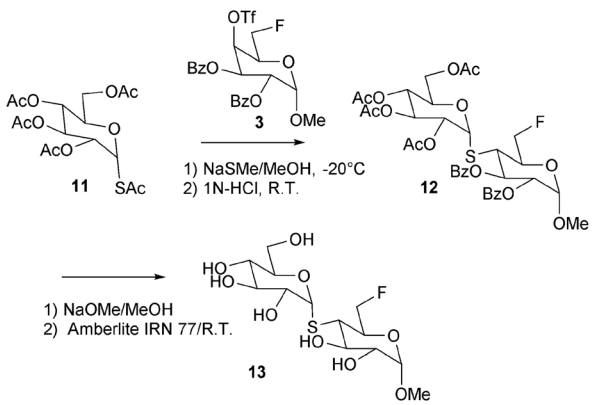

Scheme 3 Synthesis of methyl 6-deoxy-6-fluoro-4-thio-α-D-maltoside (**13**).

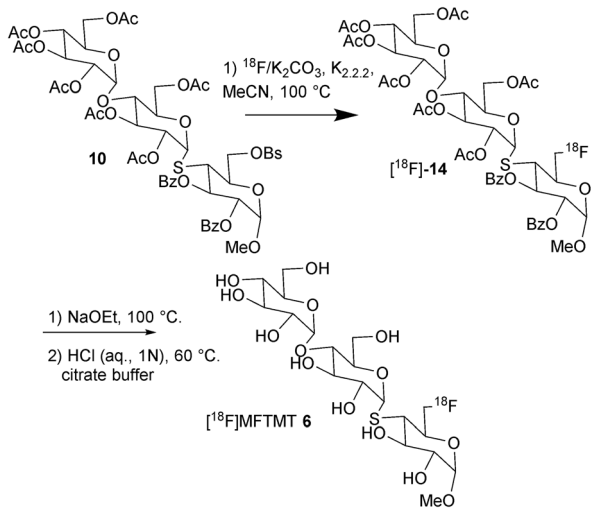

Scheme 4 Synthesis of [^{18}F]MFTMT ([^{18}F]**6**).

Compound [^{18}F]**6**, ([^{18}F]MFTMT) was obtained by sequentially reacting **10** with K^{18}F/Kryptofix-222, complex in CH_3CN at 100 °C, followed by the removal of the acetate and benzoate groups of [^{18}F]**14** with using sodium ethoxide (NaOEt–)–ethanol (EtOH) at 100 °C. Following the removal of the maltriose-protecting groups, the reaction mixture was neutralized, and [^{18}F]MFTMT was purified by semi-preparative high-performance liquid chromatography (HPLC) using 6% EtOH–water as the eluent. The product was sterilized by passing through a Millex®-GS sterile filter (0.22 μm). A total of 188 mCi (6956 MBq) of [^{18}F]MFTMT in a decay-corrected radiochemical yield (RCY) of 20% was obtained from 1.56 Ci, 57.72 GBq of [^{18}F]-fluoride in a synthesis time of 80 min. The purified final product [^{18}F]MFTMT was diluted in a saline solution (pH = 6) and used for *in vitro* and positron emission tomography (PET) imaging studies. Radiochemical and chemical purity were >95% and the specific activity = 1.9 Ci (70.3 GBq) per μmol (ESI Fig. S1†).

[^{18}F]MFTMT was identified by co-injection with non-radiolabeled MFTMT ([^{19}F]MFTMT (**6**)) by HPLC analysis using a Waters reverse phase analytical HPLC column (ESI Fig. S2†).

Biological evaluation of [^{18}F]MFTMT

To understand biological characteristics of [^{18}F]MFTMT, we evaluted the uptake of [^{18}F]MFTMT by bacteria and mammlian cells *in vitro*. The efficacy of [^{18}F]MFTMT to detect bacterial infection was determined by [^{18}F]MFTMT PET imaging.

Bacteria uptake assays

The affinity of [^{18}F]MFTMT was evaluated using bacteria and mammalian cells. Fig. 1a shows that *S. aureus* internalized [^{18}F]MFTMT, whereas *E. coli* did not. The numerical values of uptake of radioactivity by bacteria and CHO-K1 cells are shown in ESI Table S1.† The level of radioactivity internalized by 1×10^8 colony-forming units (CFU) of *S. aureus* after incubation with 5 to 20 μCi mL^{-1} of [^{18}F]MFTMT was increased with the loading radioactivity. The K_m and V_{max} of *S aureus* with [^{18}F]MFTMT was calculated as

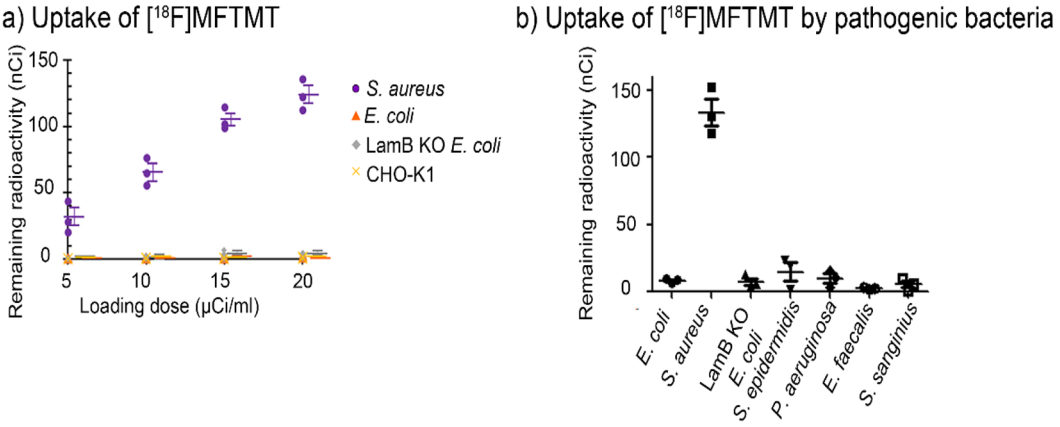

Fig. 1 Uptake of [^{18}F]MFTMT. (a) Uptake of [^{18}F]-MFTMT by bacteria and CHO-K1 cells. Bacteria, *E. coli*, *S. aureus*, and LamB mutant *E. coli* (LamB KO *E. coli*), and CHO-K1 cells were incubated with [^{18}F]MFTMT at concentrations of 5, 10, 15, and 20 μCi mL^{-1} for 1 h. *S. aureus* internalized [^{18}F]MFTMT, while *E. coli*, LamB KO *E. coli*, and CHO-K1 cells did not internalize [^{18}F]MFTMT. (b) Uptake of [^{18}F]MFTMT by common pathogens for implantable medical device infection, *Staphylococcus epidermidis* (*S. epidermidis*), *Pseudomonas aeruginosa* (*P. aeruginosa*), *Enterococcus faecalis* (*E. faecalis*) and *Streptococcus sanguinis* (*S. sanguinis*), were evaluated. Bacteria were incubated with 20 μCi mL^{-1} of [^{18}F]MFTMT for 1 h, and the remaining radioactivity was evaluated. Only *S. aureus* internalized significant radioactivity, on the other hand, other bacteria internalized minimal radioactivity.

$K_m = 151.2 \pm 224.7$ nCi and $V_{max} = 18.1 \pm 24.3$ nCi min^{-1}/10^8 CFU by using the Prism software. In contrast, the observed radioactivity in *E. coli*, LamB KO *E. coli*, and CHO-K1 cells was nearing the detection limitation of radioactivity even after incubation with 20 μCi mL^{-1} of [^{18}F]MFTMT. These results showed that while *S. aureus* internalized [^{18}F]MFTMT, *E. coli* and mammalian cells internalized minimal amounts of this compound.

We further evaluated if other pathogenic bacteria for implantable medical device infections internalized [^{18}F]MFTMT.[43–45] As shown in Fig. 1b, *S. aureus* significantly internalized [^{18}F]MFTMT (133.3 ± 10.0 nCi). On the other hand, the retained amounts of [^{18}F]MFTMT in bacteria other than *S. aureus* were small, and no significant differences were observed. These results showed that [^{18}F]MFTMT specifically accumulates in *S. aureus* but not in other bacteria. The numerical values of uptake of radioactivity by bacteria are shown in ESI Table S2.† showed that while *S. aureus* internalized [^{18}F]MFTMT, *E. coli* and mammalian cells internalized minimal amounts of this compound.

We further evaluated if other pathogenic bacteria for implantable medical device infections internalized [^{18}F]MFTMT.[43–45] As shown in Fig. 1b, *S. aureus* significantly internalized [^{18}F]MFTMT (133.3 ± 10.0 nCi). On the other hand, the retained amounts of [^{18}F]MFTMT in bacteria other than *S. aureus* were small, and no significant differences were observed. These results showed that [^{18}F]MFTMT specifically accumulates in *S. aureus* but not in other bacteria. The numerical values of uptake of radioactivity by bacteria are shown in ESI Table S2.†

In the uptake studies with bacteria and CHO-K1 cells, both [^{18}F]MFTMT showed high selectivity for *S. aureus* compared with mammalian cells and pathogenic bacteria other than *S. aureus*.

In vivo PET imaging of rat skin pocket infections using [^{18}F]MFTMT

We evaluated the accumulation of [^{18}F]MFTMT in a rat skin-pocket-infection model.[18] To examine whether the selectivity of [^{18}F]MFTMT for *S. aureus* is maintained *in vivo*, we used four groups, control, *E. coli* infected, *S. aureus* infected and non-infectious inflammation groups. At the time of PET imaging, the body weight of rats was 298.0 ± 3.6 g and the amount of injected radioactivity per gram was 0.84 ± 0.02 μCi g^{-1}. The body weight and dosage of radioactivity showed no significant differences between the four groups (ESI Fig. S11†).

To understand the basic characteristics of [^{18}F]MFTMT PET imaging, we evaluated the distribution of radioactivity in the control rats. The accumulation of radioactivity in the major organs and tissue was calculated as standardized uptake value (SUV), and the SUV of the organs and tissue were compared. The kidneys showed the highest accumulation which was significantly increased compared with other organs and tissue, suggesting that the radiotracer is excreted *via* the kidneys. Among the organs and tissue excluding the kidney, the liver showed significantly increased accumulation of radioactivity compared with other organs and tissue (ESI Fig. S12†). These results suggest that the majority of [^{18}F]MFTMT and its metabolite were excreted into urine *via* the kidneys and feces *via* the liver. Other than these metabolic organs, the brain, skeletal muscles, and the subcutaneous fat and soft tissue showed significantly reduced accumulation compared with the blood. In our studies, the ratio of free [^{18}F] was less than 4%, thus, although some non-specific accumulation in the bones was observed, it was not significantly increased compared to the radioactivity in the blood. These findings show that the distribution of radioactivity derived from [^{18}F]MFTMT is not evenly distributed in the body and that to evaluate the accumulation of the tracer induced by bacterial infection, the radioactivity in the target lesion should be compared with that in the non-infected area of the same organ/tissue.

Despite demonstrating specificity in *in vitro* uptake studies with bacteria and mammalian cells, Fig. 2a shows the accumulation of radioactivity not only in the *S. aureus*-infected

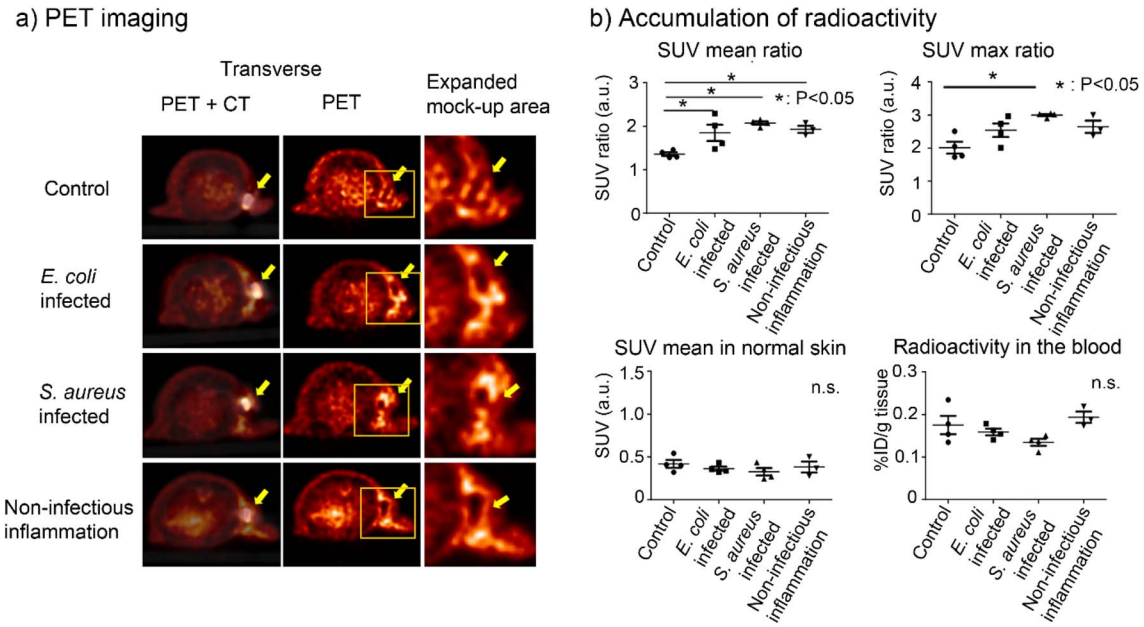

Fig. 2 [^{18}F]MFTMT PET imaging of device infection model in rats. (a) [^{18}F]MFTMT PET imaging was conducted on a skin-pocket-infection model in rats, utilizing sum images from 30 to 60 min for evaluation. The location of the mock-up was confirmed by merging images of PET and CT. Coronal and sagittal sections of PET images are shown in the ESI Fig. S12.† No radioactivity accumulation was observed in the mock-up area in the control rats. Radioactivity accumulated not only in the mock-up area in *S. aureus*-infected rats but also in *E. coli*-infected rats and rats with non-infectious inflammation. Arrows show mock-up areas. (b) Radioactivity accumulation around the mock-up area and normal skin was compared using the ratio of SUV in the mock-up area and normal skin area. The mean SUV ratio in the mock-up area was significantly increased in *S. aureus*-infected rats, *E. coli*-infected rats, and non-infectious inflammation rats compared to control rats. SUV max ratio was increased in *S. aureus*-infected rats. SUVs in the normal skin area were similar across the four groups. The remaining radioactivity in the blood was evaluated by placing the ROI on the left ventricle, indicated as a ratio to the injected radioactivity (% ID per g tissue). * Indicates $p < 0.05$.

group but also in the *E. coli*-infected and non-infectious inflammation groups. The PET imaging of coronal and sagittal views is shown in the ESI Fig. S12.† The accumulation of radioactivity in mock-up areas were compared using the ratio of SUV of the mock-up area to that of the normal skin area. The average accumulation of radioactivity in the mock-up area (SUV mean ratio) was significantly increased in the *E. coli*-infected, *S. aureus*-infected, and non-infectious inflammation groups compared with the control group (Fig. 2b). The highest radioactivity in the region of interest (ROI) (SUV max ratio) in the *S. aureus*-infected group was significantly increased compared to the control group, representing a 1.49-fold increase. The SUV max ratios of the *E. coli*-infected and non-infectious inflammation groups did not significantly differ from the *S. aureus*-infected group. The radioactivity in the normal skin area did not differ among these four groups. The numeric values of PET imaging analysis are shown in ESI Table S3.† These results suggest that both *S. aureus* and the inflammatory tissue of rats accumulated [^{18}F]MFTMT and/or its metabolite(s).

Blood radioactivity was also assessed by placing the ROI within the left ventricle in a coronal view to estimate blood radioactivity retention in rats. The remaining radioactivity in the blood was calculated as a ratio relative to the injection dose per gram (% ID per g tissue). At the time of imaging, the remaining radioactivity in the blood showed no significant difference in the four groups (Fig. 2b).

Our previous study with the same device infection model showed that [^{18}F]FDG significantly accumulated both in the *S. aureus* infected and non-infectious inflammation lesions compared with control lesions (SUV mean ratios 2.86, 2.62 and 1.54, respectively).[18] On the other hand, [^{18}F]MHF accumulated only in the *S. aureus* infected lesion compared with non-infectious inflammation and control lesions (SUV mean ratio 2.87, 1.26 and 1.61, respectively), and different from [^{18}F]FDG PET imaging, [^{18}F]MHF showed obvious selectivity for bacteria.[18] To explore why [^{18}F]MFTMT lost the selectivity to *S. aureus* in *in vivo* imaging, we further investigate the *in vitro* and *in vivo* metabolites of [^{18}F]MFTMT and possible transporters in mammalian cells.

In vitro and *in vivo* metabolite(s) of [^{18}F]MFTMT

***In vitro* metabolite(s) of [^{18}F]MFTMT.** The stability of [^{18}F]-MFTMT ([^{18}F]**6**) in 2% EtOH–phosphate-buffered saline (PBS), rat serum, and human serum. [^{18}F]MFTMT exhibited stability even after 3.5 h of incubation (Fig. 3a). The percentage of intact [^{18}F]MFTMT in rat and human serum at 37 °C after 5 to 30 min of incubation was determined by comparing HPLC retention times of [^{18}F]MFTMT to [^{18,19}F]**13** ([^{18,19}F]-methyl 6-deoxy-6-fluoro-4-thio-α-D-maltoside, [^{18,19}F]MFTM), using HPLC. In rat serum, the conversion of [^{18}F]MFTMT to [^{18,19}F]MFTM was 45% ± 1% (number of samples, $N = 3$) after 5 min, 95% ± 1% ($N = 3$) after 15 min, and 100% ($N = 3$) after 30 min (Fig. 3b). No further

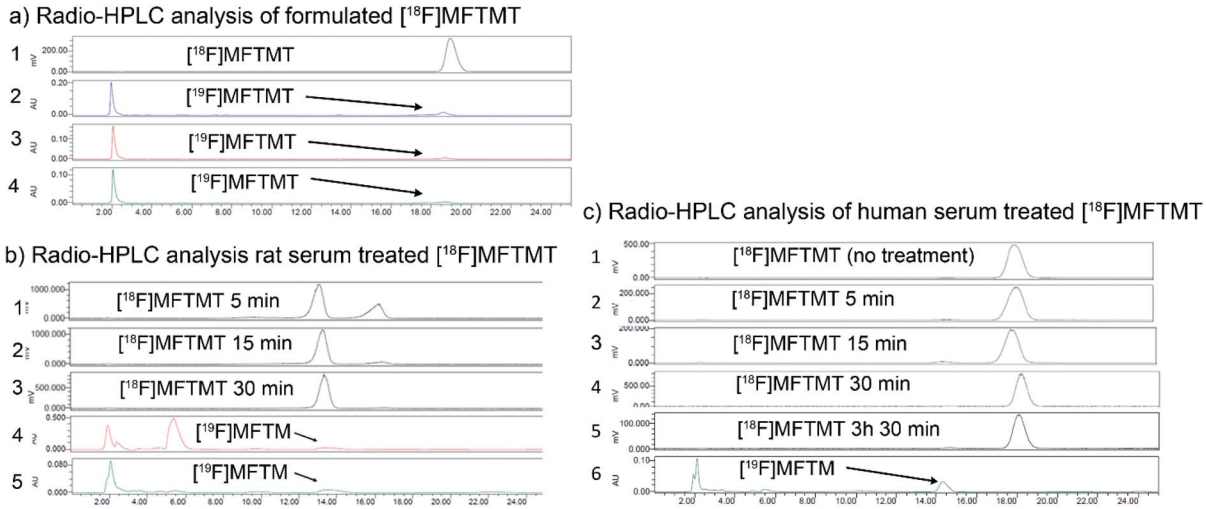

Fig. 3 *In vitro* metabolite(s) of [^{18}F]MFTMT. (a) Sample chromatograms of the radiometric HPLC analysis of formulated [^{18}F]MFTMT. [^{18}F]MFTMT was injected into a reversed-phase (RP)-HPLC system. (1) [^{18}F]-radioactivity, (2) UV absorbance at 215 nm, and (3) UV absorbance at 195 nm, (4) UV absorbance at 205 nm. The identity of [^{18}F]MFTMT ($R_t = 20$ min) was confirmed by co-injection of non-radiolabeled [^{19}F]MFTMT ($R_t = 20$ min) into an RP-HPLC system. (b) Chromatograms of the radiometric HPLC analysis of formulated [^{18}F]MFTMT ($R_t = 17$ min) following incubation in rat serum. [^{18}F]MFTM ($R_t = 14$ min) was identified by co-injection of non-radiolabeled [^{19}F]MFTM ($R_t = 14$ min) into an RP-HPLC system. (1) [^{18}F]-radioactivity at 5 min of incubation, (2) [^{18}F]-radioactivity at 15 min of incubation, (3) [^{18}F]-radioactivity at 30 min of incubation, (4) UV absorbance at 195 nm + co-injection [^{19}F]MFTM at 30 min, and (5) UV absorbance at 205 nm + co-injection [^{19}F]MFTM at 30 min. (c) Chromatograms of the radiometric HPLC analysis of formulated [^{18}F]MFTMT ($R_t = 19$ min) following incubation in human serum. The absence of the formation of [^{18}F]MFTM was identified by co-injection of non-radiolabeled [^{19}F]MFTM ($R_t = 15$ min) into an RP-HPLC system. (1) [^{18}F]MFTMT dose, (2) [^{18}F]-radioactivity at 5 min of incubation, (3) [^{18}F]-radioactivity at 15 min of incubation, (4) [^{18}F]-radioactivity at 30 min of incubation, (5) [^{18}F]-radioactivity at 3.5 hours of incubation, and (6) UV absorbance at 205 nm + co-injection [^{19}F]MFTM ($R_t = 15$ min) at 30 min.

digestion of [^{18}F]MFTM was observed in the rat serum. On the other hand, in both female and male human serum, [^{18}F]MFTMT remained unchanged at 5, 15, 30 min, and 3.5 hours (Fig. 3c). Serum enzymes potentially involved in metabolizing [^{18}F]MFTMT are α-glucosidase and α-amylase. This study demonstrates that rat and human serum metabolize [^{18}F]MFTMT differently. This suggests that rat serum contains α-glucosidase which hydrolyses one glucose unit of oligosaccharides from the non-reducing end, and this enzyme is responsible for the metabolism of [^{18}F]MFTMT to [^{18}F]MFTM.[33–36] Furthermore, the detection of only one radiometabolite, [^{18}F]**13** ([^{18}F]MFTM), demonstrates the effectiveness of the 1,4-α-thio-linkage in preventing α-glucosidase metabolism of [^{18}F]MFTM to methyl 6-deoxy-6-[^{18}F]fluoro-D-glucopyranoside or methyl 4-thio-6-deoxy-6-[^{18}F]fluoro-D-glucopyranoside. Interestingly, [^{18}F]MFTMT was not metabolized in human serum. This finding suggests that if mammalian cells may accumulate [^{18}F]MFTM but not [^{18}F]MFTMT, [^{18}F]MFTMT is still a promissing candidate for bacteria-specific PET imaging for human beings.

***In vivo* metabolite(s) of [^{18}F]MFTMT.** To evaluate whether another radioactive metabolite, such as methyl 6-deoxy-6-[^{18}F]fluoro-α-D-glucopyranoside, might be generated *in vivo*, we analyzed the tissue extracts from the non-infectious inflammation rats injected with [^{18}F]MFTMT 1 h after injection of the tracer. Urine was not sampled because of technical reasons. As shown in Fig. 4, no [^{18}F]MFTMT was observed in the samples but the radioactive peaks matched with [^{19}F]MFTM. This result shows that [^{18}F]MFTMT was only metabolized into [^{18}F]MFTM within 1 h from the injection, and no other glucose analogues with [^{18}F] were generated.

Uptake of serum treated [^{18}F]MFTMT and [^{18}F]MFTM by bacteria

We investigated whether [^{18}F]MFTM, the metabolite of [^{18}F]FMTMT, was still selective for *S. aureus*. Fig. 5a shows the uptake of serum treated [^{18}F]MFTMT by bacteria and CHO-K1 cells. The numerical values of uptake of radioactivity by bacteria and CHO-K1 cells are shown in ESI Table S4.† Similar to non-processed [^{18}F]MFTMT, *S. aureus* internalized serum treated [^{18}F]MFTMT. Because of the large dispersion of data at each concentration, the kinetics could not be calculated. On the other hand, *E. coli*, LamB KO *E. coli*, and CHO-K1 cells showed minimal internalization of radioactivity even when incubated with 15 μCi mL^{-1} of serum-treated [^{18}F]MFTMT. These results show that both [^{18}F]MFTMT and its serum metabolite, [^{18}F]MFTM, are only internalized by *S. aureus*.

We also evaluated whether [^{18}F]MFTM was internalized common pathogens for implantable device infections. The purity of [^{18}F]MFTM was confirmed by HPLC (ESI Fig. S11†). Fig. 5b shows that similar to [^{18}F]MFTMT, *S. aureus* significantly internalized [^{18}F]MFTM (123.1 ± 7.7 nCi), but bacteria other than *S. aureus* internalized little of [^{18}F]MFTM with no significant differences in each other. The numeric values of uptake of [^{18}F]MFTM are shown in the ESI Table S5.† These results showed that the selectivity of [^{18}F]MFTM to *S. aureus*.

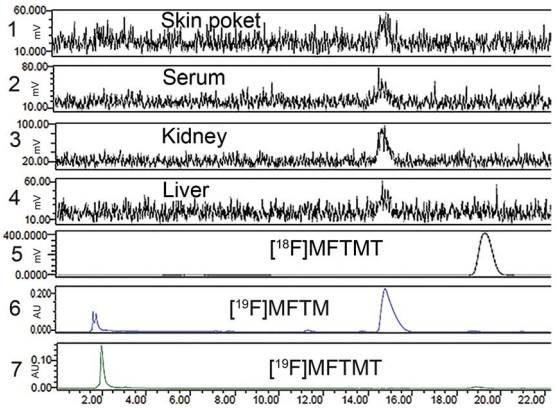

Fig. 4 *In vivo* metabolite(s) of [^{18}F]MFTMT. Non-infectious inflammation model rats were sacrificed 1 h after injection of [^{18}F]MFTMT. The extracted tissue and organs were homogenized, and the extracted samples were analyzed by radiometric HPLC. (1) skin pocket, (2) serum, (3) kidney, (4) liver, (5) [^{18}F]MFTMT, (6) [^{19}F]MFTM (cold standard) and (7) [^{19}F]MFTMT (cold standard). Samples (1) to (4) have one peak that matches with [^{19}F]MFTM, showing [^{18}F]MFTM is the only radioactive metabolite of [^{18}F]MFTMT *in vivo*.

Sodium glucose co-transporter (SGLT) 1 is the potential cause of [^{18}F]MFTMT accumulation in inflamed tissue

We explored the underlying reasons for the accumulation of radioactivity derived from [^{18}F]MFTMT in mammalian tissue. [^{18}F]MFTMT and its metabolite, [^{18}F]MFTM, possess glucoside structures. Therefore, we hypothesized that glucose transporters might be involved in the unexpected accumulation of radioactivity observed in *E. coli*-infected rats and rats with non-infectious inflammation.

In mammalian tissue, glucose is transported through glucose transporters (GLUTs) and sodium–glucose co-transporters (SGLTs).[46–48] GLUTs are widely expressed and transport monosaccharides, such as glucose and fructose, while they do not transport disaccharides and longer maltodextrins.[48–50] GLUTs are also sensitive to the modification on the anomeric carbon and do not transport α-methyl-D-glucoside.[46,51] Conversely, SGLTs are expressed in specific tissues and organs, such as the intestine, kidneys, and liver.[52–56] As shown in Fig. 3a, radioactivity accumulation was localized in the inflammatory area, liver, and kidneys, suggesting that GLUTs might not contribute to this unexpected radioactivity accumulation. Thus, we evaluated whether SGLTs, the alternative glucose transport system in mammalian tissue, were expressed in the region around the mock-ups, and whether SGLT1 and SGLT2 interact with [^{18}F]MFTMT and [^{18}F]MFTM, the metabolite of [^{18}F]MFTMT.

Expression of SGLT1 and SGLT2 around the mock-up area

We evaluated the expression of SGLT1 and SGLT2 around the mock-ups by immunohistochemistry and quantitative polymerase chain reaction (qPCR). Fig. 6a and b show that both SGLT1 and SGLT2 are highly expressed in fibroblasts (vimentin-positive cells) within the inflammatory area, respectively.

In qPCR analysis, the expression of SGLT1 and SGLT2 was evaluated by expression relative to β-actin. As shown in Fig. 7, the messenger ribonucleic acid (mRNA) for SGLT1 and SGLT2 in the inflammatory tissues were significantly increased compared to the tissue from the control animals.

Interaction of [^{18}F]MFTMT and [^{18}F]MFTM with SGLTs

To investigate the potential involvement of SGLTs in the accumulation of radioactivity derived from [^{18}F]MFTMT, we established CHO-K1 cells expressing human SGLT1 (CHO-K1-hSGLT1) and SGLT2 (CHO-K1-hSGLT2).[57–59] The functional expression of these genes was confirmed by measuring the uptake of 1-NBDG, a fluorescent substrate specific for SGLT1 and SGLT2 (Fig. 8a).[60]

As shown in Fig. 8b, the remaining radioactivity in CHO-K1-hSGLT1 cells incubated with [^{18}F]MFTMT was 4.0 nCi which was significantly higher than that in control CHO-K1 cells and

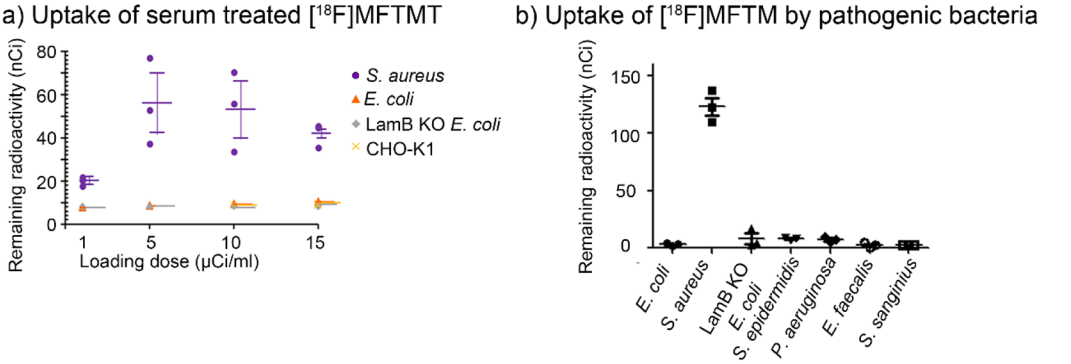

Fig. 5 Uptake of serum treated [^{18}F]MFTMT and [^{18}F]MFTM. (a) Uptake of serum treated [^{18}F]-MFTMT by bacteria and CHO-K1 cells. Bacteria, *E. coli*, *S. aureus*, and LamB mutant *E. coli* (LamB KO *E. coli*), and CHO-K1 cells were incubated with the rat serum-treated [^{18}F]MFTMT at concentrations of 1, 5, 10, and 15 μCi mL^{-1} for 1 h. Consistent with the uptake study with [^{18}F]MFTMT, only *S. aureus* internalized serum-treated [^{18}F]MFTMT. (b) Uptake of [^{18}F]MFTM by common pathogens for implantable medical device infection, *Staphylococcus epidermidis* (*S. epidermidis*), *Pseudomonas aeruginosa* (*P. aeruginosa*), *Enterococcus faecalis* (*E. faecalis*) and *Streptococcus sanguinis* (*S. sanguinis*), were evaluated. Bacteria were incubated with 20 μCi mL^{-1} of [^{18}F]MFTM 1 h, and the remaining radioactivity was evaluated. Similar to the uptake of [^{18}F]MFTMT, only *S. aureus* internalized massive radioactivity.

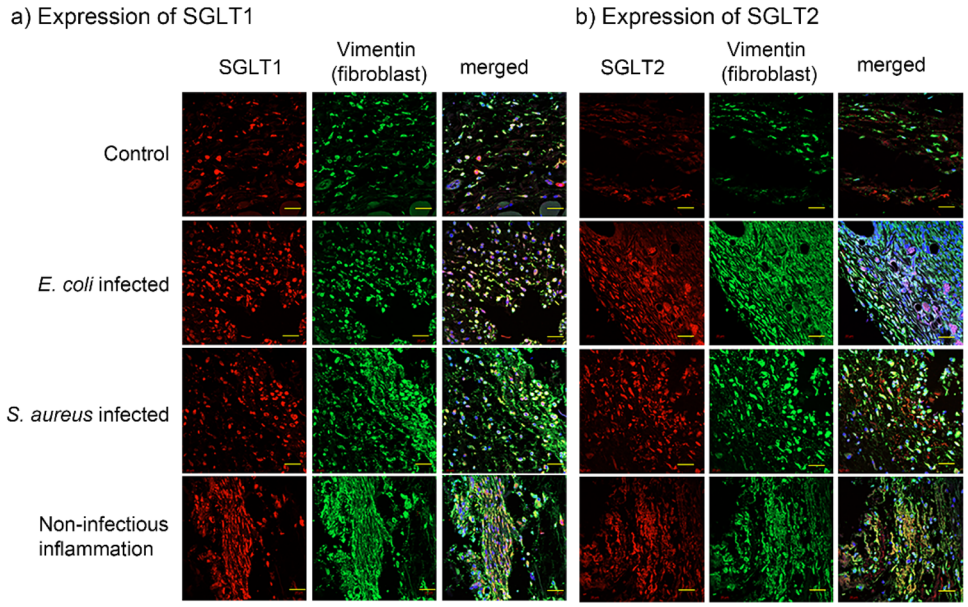

Fig. 6 Immunohistochemistry on tissue around the skin pocket. Expression of SGLT1 and SGLT2 in the mock-up area was evaluated by immunohistochemistry. (a) SGLT1 (red) was expressed on fibroblasts (green, vimentin-positive cells), which exhibited an increase in the inflammatory tissue. (b) Similarly, SGLT2 (red) was expressed on fibroblasts (green). The scale bars represent 40 μm.

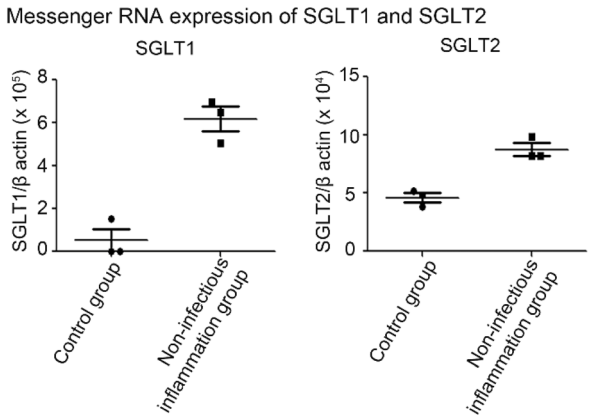

Fig. 7 Expression of SGLT1 and SGLT2 in the skin pocket from the control group and from the non-infectious inflammation group was quantified with qPCR. The expression of the target genes is indicated as the ratio to β-actin, a house keeping gene. Expression of SGLT1 in the non-infectious inflammation group was about 12 times that of the control group. Expression of SGLT2 in the non-infectious inflammation group was about 1.8 times the control group.

CHO-hSGLT2 cells. Similar to the cells exposed to [^{18}F]MFTMT, the remaining radioactivity in the CHO-K1 hSGLT1 cells incubated with [^{18}F]MFTM was 5.1 nCi which was significantly increased compared with CHO-K1 control and CHO-K1 hSGLT2 cells (Fig. 8c). The retention of [^{18}F]MFTMT and [^{18}F]MTM in CHO-K1-hSGLT1 cells was approximately 3.3 times and 3.2 times that of control CHO-K1 cells, respectively. Moreover, the retention of radioactivity in CHO-K1 hSGLT1 cells treated with mizagliflozin, a specific SGLT1 inhibitor, was significantly suppressed (Fig. 8b and c). The numeric values of remaining radioactivity in the CHO-K1 cells are shown in ESI Table S6.†

These results demonstrate that SGLT1 is highly expressed in inflammatory tissue and is potentially involved in the accumulation of [^{18}F]MFTMT and [^{18}F]MFTM, likely elucidating the loss of specificity of [^{18}F]MFTMT and [^{18}F]MFTM observed *in vivo* despite its specificity *in vitro*.

Discussion

We synthesized [^{18}F]MFTMT and assessed its uptake by bacteria, its stability against enzymatic digestion, and its effectiveness at detecting bacterial infections both *in vitro* and *in vivo*.

Inflammatory tissue, serum, and the drug-metabolizing organs, the liver and kidneys. Our findings suggest that α-glucosidase can digest the glycosyl bond, while the thio-glycosyl bond demonstrates resistance to enzymatic digestion for at least 1 hour.

Our *in vitro* uptake experiments revealed that *S. aureus* internalized both [^{18}F]MFTMT and [^{18}F]MFTM, on the other hand, other bacteria and mammalian cells internalized minimal amounts of [^{18}F]MFTMT and [^{18}F]MFTM. [^{18}F]MFTMT has three characteristic modifications from maltotriose, a (1–4)-thio-glycosyl bond, 6-deoxy-6-fluoro modification, and -*O*-methyl modification on the anomeric carbon. [^{18}F]MFTM, the metabolite of [^{18}F]MFTMT also has the same modifications. Among the bacteria used for this study, the maltose/maltodextrin transport systems in *E. coli* have been extensively studied providing insight into how these modifications can affect transport into *E. coli*.[20–22,61–79] In *E. coli*, the maltoporin, LamB, situated on the outer membrane, initially allows the permeation of maltodextrins into the periplasmic space.[67–74] Inside the periplasmic space, the maltose/maltodextrin-binding protein, malE, binds to

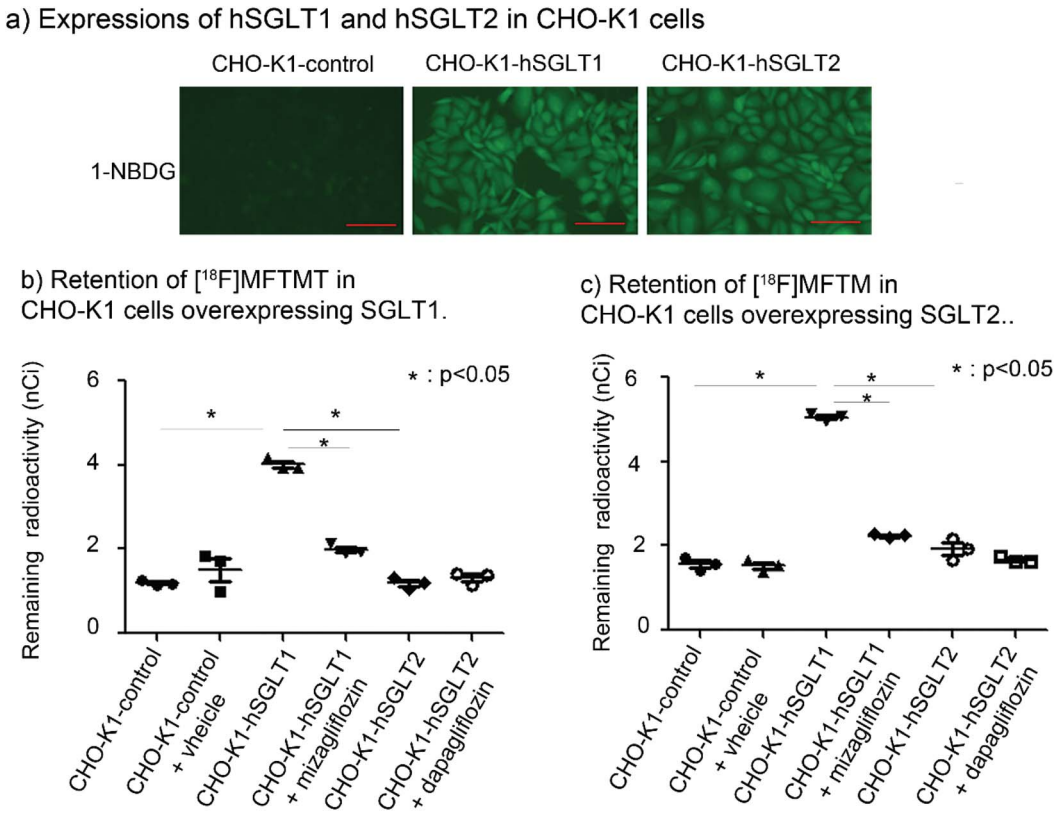

Fig. 8 Accumulation of [^{18}F]MFTMT and derivative of [^{18}F]MFTMT by SGLT1. (a) Stable expression of human SGLT1 (hSGLT1) or SGLT2 (hSGLT2) was established in CHO-K1 cells. CHO-K1-hSGLT1 and CHO-K1 hSGLT2 cells internalized 1-NBDG, a specific substrate for SGLT1 and SGLT2. Scale bars represent 100 μm. (b) Retention of [^{18}F]MFTMT and (c) retention of [^{18}F]MFTM by CHO-K1 cells overexpressing SGLTs. CHO-K1-hSGLT1, hSGLT2, and control cells were incubated with 20 μCi mL^{-1} of [^{18}F]MFTMT for 1 h, and the remaining radioactivity was evaluated. Some cells were treated with vehicle, mizagliflozin, a specific SGLT1 inhibitor, or dapagliflozin, a specific SGLT2 inhibitor. Retention of both [^{18}F]MFTMT and [18F]MFTM in CHO-K1-hSGLT1 cells were significantly higher compared to CHO-K1-hSGLT2 and control cells, and mizagliflozin significantly suppressed the retention of [^{18}F]MFTMT and [^{18}F]MFTM.

maltodextrins (forming malE-maltodextrin complex).[62–64,66,67] Subsequently, the malE-maltodextrin complex associates with the maltodextrin transporter (malF–malG–malK complex) on the inner membrane, facilitating maltodextrin transport into the cytoplasm.[62,63] LamB and malF in the malF–malG–malK complex recognize the non-reducing end of maltodextrins, while malE recognizes its reducing end.[62–64,66–74] Studies have shown that modifications on the reducing end of maltodextrin can considerably influence malE binding.[62–65] Our first generation [^{18}F]-maltodextrin probe, [^{18}F]MHF, featuring [^{18}F]fluorine attached *via* a β-glycosidic linkage on the anomeric carbon at the reducing end of maltohexaose, was internalized by both *S. aureus* and *E. coli*.[16–18] This suggests that malE of *E. coli* may tolerate only one modification on the anomeric carbon at its reducing end. MalE of *E. coli* binds to maltose and maltodextrins up to maltoheptaose.[67,80,81] Crystallography studies showed that malE of *E. coli* generates hydrogen bonds with the hydroxyl groups on glucose molecule at the reducing end and the hydroxyl groups on 2, 3, and 6 positions of the glucose molecule next to the reducing end.[62,65] When malE of *E. coli* binds to maltotriose or longer maltodextrins, the number of hydrogen bonds generated between malE of *E. coli* and maltodextrins increases, while the binding positions malE of *E. coli* and two glucose molecules from the reducing end are maintained.[62,65] This binding to maltose or two glucose molecules from the reducing end induces conformational change of malE of *E. coli*, making malE of *E. coli* the "closed" conformation.[82,83] MalE of *E. coli* also known to bind modified maltodextrin analogs such as maltotetraiol. However, the binding conformation remains in the "open" form which is considered as non-functional for transport.[64] The carbon–sulfur bond distance in thio-glycosyl bond is longer than the carbon–oxygen bond in the glycosyl bond, resulting in a distinct relative position of the glucose molecule next to the reducing end glucose molecule compared to maltose and maltodextrins.[84,85] Consequently, with the 6-deoxy-6-fluoro modification, [^{18}F]MFTMT might exhibit reduced affinity to the malE of *E. coli*.

PTS of *E. coli* also transports maltose from the periplasmic space to the cytosol.[75–79]. [^{18}F]MFTM, the radioactive metabolite of [^{18}F]MFTMT and a maltose analog, was considered as the potential substrate for PTS. However, in PTS, the enzyme IIC component (EIIC) corresponding to maltose is located on the inner membrane, and a crystallography study by McCoy *et al.* showed that it recognizes the hydroxyl groups on the 6- and 6′-carbons.[77–79] Thus, 6-deoxy-6-fluoro-modification in [^{18}F]MFTM, the maltose analog, appears to be critical for binding to ECII for maltose.

The maltose/maltodextrin transport systems, maltodextrin transporter and PTS, in pathogenic bacteria other than *E. coli* still need to be elucidated. However, our results suggest that the maltodextrin binding protein and ECII for maltose in the evaluated bacteria, *Pseudomonas aeruginosa*, *Staphylococcus epidermidis*, *Streptococcus sanguinis* and *Enterococcus faecalis*, may also be sensitive to the modifications on the reducing end.

In contrast, *S. aureus* internalized both [^{18}F]MFTMT and [^{18}F]MFTM. This finding implies that the maltose and maltodextrin transportation systems in *S. aureus* employ different substrate-binding mechanisms from that of *E. coli*. Abbott *et al.* elucidated sugar utilization in *Streptococcus pneumoniae* and demonstrated that the maltodextrin binding protein of *Streptococcus pneumoniae* binds to maltotriose and longer maltodextrins. They also showed that PTS transports glucose, maltose and maltotriose, and that the binding conformation of the maltodextrin binding protein with maltoheptaose is different compared to malE in *E. coli*.[23] We recently found that the maltodextrin-binding protein of *S. aureus* exhibits different binding thermodynamics compared with that of *E. coli* and like that of *S. pneumonia* and that it functionally binds to maltotriose and longer maltodextrins.[81] Other studies also show that maltodextrin binding proteins of Gram-positive bacteria bind to maltotriose and longer maltodextrins, and PTS of Gram-positive bacteria transports glucose, maltose and maltotriose.[86–91] These findings suggest that [^{18}F]MFTMT can be transported *via* maltodextrin transporter and PTS, and [^{18}F]MFTM can be transported by PTS in *S. aureus*. We did not specify whether the maltodextrin transporter or PTS in *S. aureus* internalized [^{18}F]MFTMT and/or its metabolite, [^{18}F]MFTM. However, our results suggest that maltodextrin transporter and/or PTS in *S. aureus* are tolerant to the modifications on the reducing end and have different binding affinities and mechanisms to substrates compared to those in *E. coli*. Our results indicated that the tolerance of maltodextrin transporter and PTS to the modifications on maltose/maltodextrins is different in bacterial species. This finding suggests the possibility to target specific bacterial species using modifications of maltodextrin-based probes. Future studies will explore potential differences in maltodextrin transporters between *S. aureus*, other pathogenic bacteria and *E. coli*.

[^{18}F]FDG is assumed to be uniformly distributed in the body with increased accumulation of radioactivity indicating increased glucose uptake caused by pathological or physiological changes, such as tumors, inflammation, and muscle activities.[92,93] In contrast, the concept of maltodextrin-based imaging probes is that maltodextrin-based imaging probes are only internalized by bacteria and not by mammalian cells.[16–18] The injected [^{18}F] labeled maltodextrin-based imaging probes are expected to be rapidly distributed from the blood to interstitial fluid, accumulate in the metabolic organs, and are excreted into urine without being internalized by other tissue and organs. As a result, the remaining radioactivity in the blood and interstitial fluid, which is detected as background is very low, emphasizing the accumulation of radioactivity in bacteria, even if the absolute quantity of radioactivity is small. Therefore, evaluating and understanding whether and how [^{18}F] labeled maltodextrin-based imaging probes and their metabolites accumulate in normal and inflammatory tissue in *in vivo* is important. To clarify the accumulation of radioactivity in the target area, we used the SUV ratios, the relative the accumulation of radioactivity in the target tissue to the normal tissue, to compare the accumulation of radioactivity between the experimental groups.

We evaluated whether [^{18}F]MFTMT and [^{18}F]MFTM accumulated in mammalian tissue. In [^{18}F]MFTMT PET imaging, we observed radioactivity accumulation not only in the *S. aureus*-infected group but also in the *E. coli*-infected and non-infected inflammation groups. Our experiments strongly suggest the involvement of SGLT1, which is highly expressed in inflammatory tissues as the cause of this false positive result. Studies showed that SGLT1 is expressed not only in the inflammatory cells but also in endothelial cells and fibroblasts and that SGLT1 is involved in inflammatory reactions.[94–98] In the *in vitro* uptake studies, when 20 μCi mL^{-1} of [^{18}F]MFTMT and [^{18}F]MFTM were loaded, the retained radioactivity in 1.2 $\times 10^5$ of CHO-K1-SGLT1 cells was about 4.0 nCi, and 5.1 nCi, respectively, which was lower than that in 1×10^8 CFUs of *S. aureus* (124 nCi). The concentration of radioactivity in the *in vivo* setting is lower than 20 μCi mL^{-1}, and it can be estimated as following. The percentage of extracellular water, including plasma and interstitial fluid, in adult rat is estimated approximately 30%.[99] Thus, in our *in vivo* experiments, when the injected radioactivity was evenly distributed in the extracellular water in the body, the concentration of radioactivity is estimated to be 2.8 μCi mL^{-1}. Assuming that the accumulation of radioactivity in *S. aureus* and CHO-K1-hSGLT1 cells obey Michaelis–Menten kinetics in which the reaction speed and substrate concentrations interacts linearly in low concentrations, the retention of [^{18}F]MFTMT and [^{18}F]MFTM in 1.2 $\times 10^5$ of SGLT1 expressing cells is estimated to be 0.56 and 0.71 nCi, respectively, and the accumulation of [^{18}F]MFTMT in 1×10^8 CFUs of *S. aureus* is estimated to be 20 times higher at 17.6 nCi. However, our study showed that inflammation increases fibroblasts expressing SGLT1 potentially leading to nonspecific accumulation of [^{18}F]MFTMT and/or [^{18}F]MFTM. This is plausible considering the high cell density of the skin at approximately 7×10^8 cells per cm^3.[100] If 1% of cells in inflammatory tissue expresses SGLT1, the retention of [^{18}F]MFTMT and [^{18}F]MFTM is estimated as 32.7 and 41.7 nCi g^{-1} tissue, respectively. Our results from immunohistochemistry and qPCR studies show that the increase of the ratio of SGLT1 expressing cells to the total cells in the inflammatory tissue is more than 10% compared to the control tissue, suggesting that the inflammatory tissue retains 327 to 417 nCi g^{-1} higher radioactivity compared with control tissue. Our skin pocket infection model contains 2.9×10^8 CUF/total infected tissue of *S. aureus*, and the expected radioactivity in the *S. aureus* infected tissue is estimated to be about 51 nCi/total infected tissue. Considering the weight of *S. aureus* infected tissue is more than 1 g and [^{18}F]MFTM has higher retention in SGLT1 over-expressing cells, the increase of radioactivity density in inflammatory tissue caused by SGLT1 might be more than 10 times compared to that by *S. aureus* infection. As a result, the accumulation of radioactivity in *S. aureus* infected area did not show a significant difference from that in other inflammation

areas induced by oil of turpentine and *E. coli* infection. We showed that inflammatory tissue expresses SGLT1, and SGLT1 is known to be expressed in many cancers.[101–103] Future study needs to ivestigate whether [^{18}F]MFTMT accumulates in cancers.

In our previous studies with [^{18}F]MHF, radioactivity accumulation was only observed in the bacteria-infected area.[16–18] In [^{18}F]MHF PET imaging with the same pocket infection model induced by *S. aureus* and non-infectious inflammation model, the SUV mean ratio in *S. aureus* infected group was significantly increased compared to control and non-infectious inflammation groups and was 1.8 times to that in control group. In contrast, [^{18}F]FDG PET imaging with the same models, the accumulation of radioactivity in both *S. aureus* infected and non-infectious inflammation lesions were significantly increased compared with that in control lesion. Different from [^{18}F]MFTMT, [^{18}F]MHF showed efficacy in *in vivo* bacteria-specific PET imaging compared with the conventional [^{18}F]FDG PET imaging.

There are several notable differences between [^{18}F]MFTMT and [^{18}F]MHF.[16–18]. [^{18}F]MHF has a maltohexaose backbone and can be digested into [^{18}F]fluoro-maltoside and [^{18}F]fluoro-maltotrioside by serum amylase and further into [^{18}F]fluoro-glucoside by serum α-glucosidase, which is highly active in rodents.[16–18,33,35,36] These metabolites, including [^{18}F]fluoro-glucoside, are not transported by GLUTs on mammalian cells because of the modification on the anomeric carbon.[46,48,50] While SGLTs can tolerate modifications on the anomeric carbon, the extended maltohexaose backbone of [^{18}F]MHF might prevent its interaction with SGLT1.[48,104–108] Despite this, the flexibility and the size of the [^{18}F]MHF linker could potentially allow for [^{18}F]fluoro-glucoside, resulting from [^{18}F]MHF degradation by serum α-glucosidase, to be transported by SGLTs. However, [^{18}F]MHF and its metabolites are swiftly excreted in the urine, leading to a rapid decline in blood radioactivity levels and minimal radioactivity accumulation in non-infectious inflammation areas.[17] Conversely, in [^{18}F]MFTMT PET imaging, blood radioactivity is sustained as compared to [^{18}F]MHF, with blood radioactivity reaching approximately 0.15% ID per g, which is more than 2.5-fold higher than that observed with [^{18}F]MHF in our previous study.[17] This difference suggests that the thio-glucosyl bond and the modification at the sixth position on the reducing end glucose in [^{18}F]MFTMT might delay its excretion and/or that of its metabolites. Furthermore, differences in the biological half-life of radioactivity might also contribute to increased radioactivity accumulation in inflammatory tissue. These results demonstrate the necessity of employing maltodextrin backbones longer than maltotriose combined with modifications to prevent enzymatic digestion, in the development of bacteria-specific imaging probes. Considering the molecular size, maltodextrin backbones with nitrogen-glycosyl bond(s) might achieve both resistance to enzymatic digestion and increased affinity for bacteria.[85]

Limitations

One limitation of this study is that we did not determine whether [^{18}F]MFTMT and [^{18}F]MFTM were transported through SGLT1 or whether they were bound to SGLT1 and were internalized by SGLT1 *via* endocytosis. Further studies will investigate the interactions between [^{18}F]MFTMT and [^{18}F]MFTM, and native maltose and maltodextrins with SGLT1. These studies will help us to optimize the maltodextrin backbone for selective bacterial imaging.

Another limitation is the use of a rat model for [^{18}F]MFTMT PET imaging. We showed that [^{18}F]MFTMT was digested into [^{18}F]MFTM by rat serum while it was stable in human serum. We conducted [^{18}F]MFTMT PET imaging to evaluate the specificity for bacteria *in vivo* because [^{18}F]MFTM was the only radioactive metabolite of [^{18}F]MFTMT *in vitro* and because [^{18}F]MFTMT and [^{18}F]MFTM had similar selectivity to bacteria *in vitro*. Rodent models are well-established and cost-effective methods to evaluate the efficacy of drugs, including imaging probes. However, understanding the differences between humans and rodents is important to evaluate the effects of the compounds. Future studyies may use other animal models or α-glucosidase inhibitor treated rats to evaluate the efficacy of maltodextrin-based imaging probes *in vivo*.

Experimental section

General information

All solvents were purchased from Biosynth, Fisher Scientific, or Sigma Aldrich and dried over 4 Å molecular sieves (8–12 mesh, Sigma Aldrich). Unless otherwise specified, all commercially available reagents and substrates were used as received. Ultra-high purity dry air was purchased from nexAir LLC. Thin-layer chromatography (TLC) was performed on Merck silica gel plates and visualized under UV light and/or H_2SO_4–EtOH. ^{1}H, ^{13}C, and ^{19}F NMR spectra were recorded on Varian Mercury 300, Bruker 600, Varian INOVA 600, INOVA 500, and INOVA 400 spectrometers. Residual solvent resonances were considered internal reference signals. ^{19}F spectra were referenced to KF. Product purification was performed *via* flash chromatography[109] unless otherwise specified. The purity and identity of compounds **2**, **3**, **5**, **6**, **8**, **9**, **10**, **12**, and **13** were determined by analytical and spectroscopical methods such as TLC, NMR, and high-resolution mass spectrometry (HRMS), and the results are shown in the Experimental Section. All the American Chemical Society (ACS) journals accept HRMS analysis of a new compound as a sufficient proof for its characterization and identity. High-resolution mass spectra were obtained from the Emory University Mass Spectroscopy Facility. [^{18}F]fluoride was produced at the Emory University Center for Systems Imaging using an 11 MeV Siemens RDS 111 negative-ion cyclotron (Knoxville, TN) by the ^{18}O(p, n) [^{18}F] reaction using [^{18}O]H_2O (95%). Trap/release cartridges model DW-TRC were purchased from D&W, Inc. (Oakdale, TN). Radiometric TLC was performed with the same type of silica plates from Whatman and analyzed with a Raytest system (model Rita Star, Germany). Isolated radiochemical yields were determined using a dose calibrator (Capintec CRC-712M). Analytical HPLC experiments were performed using a Waters Breeze HPLC system equipped with a Bioscan flow count radioactivity detector and an inline UV detector set to monitor wavelengths at 210, 230, and 254 nm

(Atlantis T3 column, Waters; mobile phase: 6% EtOH). All animal experiments were conducted under humane conditions and were approved by the Institutional Animal Use and Care Committee and Radiation Safety Committees at Emory University. Experiments involving infectious materials were approved by the Emory University Environmental Health and Safety Office and conducted in Biosafety Level 2 (BSL-2) laboratories. The purity of all reported compounds is at least 95%, as assessed by ^{1}H NMR, radiometric TLC, or radiometric HPLC unless otherwise stated.

Chemistry

Methyl 2,3-di-*O*-benzoyl-6-deoxy-6-fluoro-α-D-galactopyranoside (2). To a stirred solution of methyl 6-deoxy-6-fluoro-α-D-galactopyranoside[38] **1** (0.65 g, 3.32 mmol) in anhydrous pyridine (1 mL) cooled to −40 °C under an argon atmosphere was added dropwise benzoyl chloride (0.86 mL, 7.3 mmol) and the reaction mixture was stirred vigorously at room temperature for 24 h under argon. The reaction was quenched by adding 0.5 N HCl (60 mL, 0 °C) and the mixture was extracted with EtOAc (20 mL × 3). The combined organic phase was washed with saturated $NaHCO_3$ (50 mL), water (50 mL), brine (50 mL) and dried over anhydrous Na_2SO_4, filtered and evaporated to dryness under the reduced pressure. The residue was purified by flash column chromatography on silica gel (CH_2Cl_2) to afford methyl 2,3-di-*O*-benzoyl-6-deoxy-6-fluoro-α-D-galactopyranoside **2** as a colorless glassy solid (0.65 g, 48.5%).

^{1}H NMR (300 MHz, $CDCl_3$): δ (ppm): 7.98 (d, 4H, J = 7.8 Hz, ArH), 7.55–7.48 (m, 2H, ArH), 7.40–7.35 (m, 4H, ArH), 5.69 (qd, 2H, J = 11.1 and 3.5 Hz), 5.20 (d, 1H, J = 14.6 Hz), 4.77 (d, 1H, J = 5.6 Hz), 4.61 (d, 1H, J = 5.6 Hz), 4.40 (s, 1H), 4.29 (d,t, 1H, J = 14.6 Hz and 5.9 Hz) 3.46 (s, 3H, OCH_3), 2.34 (d, 1H, J = 4.2 Hz).

^{13}C NMR (75 MHz, $CDCl_3$): δ (ppm): 166.3, 165.9, 133.7, 133.5, 130.1, 130.0, 129.5, 129.4, 128.7, 128.6, 97.7, 82.6 (d, $J_{C,F}$ = 169.3 Hz), 71.0, 96.0, 68.4 (d, J = 28.8 Hz), 68.3, 55.8.

HRMS (ESI) m/z found: 405.13428, calculated: 405.13441 for $C_{21}H_{22}O_7F$ $[M + H]^+$.

Methyl 2,3-di-*O*-benzoyl-4-*O*-trifluoromethylsulfonyl-6-deoxy-6-fluoro-α-D-galactopyranoside (3). To a stirred solution of methyl 2,3-di-*O*-benzoyl-6-deoxy-6-fluoro-α-D-galactopyranoside **2** (0.55 g, 1.36 mmol) in CH_2Cl_2 (10 mL) was slowly added trifluoromethanesulfonic anhydride (0.97 g, 3.4 mmol) and pyridine (0.5 mL), and the reaction mixture was stirred vigorously for 20 min at 0 °C, followed by 20 min at room temperature under argon. The reaction was quenched by adding ice water (80 mL) and the mixture was extracted with CH_2Cl_2 (50 mL × 3). The combined organic phase was washed with brine (50 mL), dried over Na_2SO_4, filtered and evaporated to dryness under reduced pressure. The residue was purified by flash column chromatography on silica gel (hexane/EtOAc, 5 : 1) to afford methyl 2,3-di-*O*-benzoyl-4-*O*-trifluoromethylsulfonyl-6-deoxy-6-fluoro-α-D-galactopyranoside (**3**) as an off white solid (0.72 g, 99%).

^{1}H NMR (300 MHz, $CDCl_3$): δ (ppm): 8.06–7.95 (m, 4H, ArH), 7.57–7.50 (m, 2H, ArH), 7.43–7.35 (m, 4H, ArH), 5.91 (dd, 1H, J = 3.5 and 10.4 Hz), 5.57 (dd, 1H, J = 3.5 and 10.4 Hz), 5.63 (d, 1H, J = 2.8 Hz), 5.63 (d, 1H, J = 4.2 Hz), 4.73–4.62 (m, 1H), 4.59–4.46 (m, 2H), 3.48 (s, 3H, OCH_3).

^{13}C NMR (75 MHz, $CDCl_3$): δ (ppm): 165.9, 165.8, 134.0, 133.8, 130.3, 130.1, 128.7, 118.5 (d, $J_{C,F}$ = 319.0 Hz), 97.6, 82.6 (d, $J_{C,F}$ = 4.6 Hz), 80.2 (d, $J_{C,F}$ = 172.7 Hz), 68.3, 67.6, 66.4 (d, $J_{C,F}$ = 25.3 Hz), 56.3.

HRMS (ESI) m/z found: 537.08411, calculated: 537.08369 for $C_{22}H_{21}O_9{}^{32}S$ $[M + H]^+$.

Methyl 2,3,4,6-tetra-*O*-acetyl-α-D-glucopyranosyl-(1–4)-*O*-(2,3,6-tri-*O*-acetyl-α-D-glucopyranosyl)-(1–4)-2,3-di-*O*-benzoyl-4-thio-6-deoxy-6-fluoro-α-D-glucopyranoside (5). To a stirred solution of 2,3,6-tri-*O*-acetyl-*S*-acetyl-(2,3,4,6-tetra-*O*-acetyl-*S*-acetyl-1-thio-α-D-glucopyranosyl)-α-D-glucopyranose[39] **4** (0.5 g, 0.72 mmol) in anhydrous MeOH (15 mL) cooled to −20 °C under an argon atmosphere was added $NaSCH_3$ (0.05 g, 0.72 mmol) and the reaction mixture was stirred at −20 °C for 3 h under argon. The reaction mixture was neutralized to pH = 7 with 1 N HCl and extracted with EtOAC (60 mL). The organic phase was washed with water (20 mL × 3), dried over Na_2SO_4, filtered, and evaporated to dryness under reduced pressure. A solution of triflate **3** (0.63, 0.72 mmol) in DMF (25 mL) and triethylamine (NEt_3 0.6 mL) was added to the thiol residue and the resulting reaction mixture was stirred at 0 °C for 1 h and 3 days at room temperature under argon. EtOAc (100 mL) was added to the reaction mixture and the EtOAC solution was washed with water (30 mL × 3), brine (30 mL) and dried over Na_2SO_4, filtered and evaporated to dryness under reduced pressure. The residue was purified by flash column chromatography on silica gel (EtOAc/hexane, 2 : 1) to afford **5** as a colorless oil (0.28 g, 37%).

^{1}H NMR (300 MHz, $CDCl_3$): δ (ppm): 7.96–7.90 (m, 4H, ArH), 7.55–7.46 (m, 2H, ArH), 7.40–7.32 (m, 4H, ArH), 6.06 (t, 1H, J = 10.4 Hz), 5.65 (d, 1H, J = 6.3 Hz), 5.41–5.34 (m, 2H), 5.22–4.93 (m, 5H), 4.87 (dd, 1H, J = 4.2 and 10.5 Hz), 4.79–4.69 (m, 2H), 4.48 (d, 1H, J = 10.2 Hz), 4.29–4.22 (m, 3H), 4.06–3.87 (m, 4H), 3.44 (s, 3H, OCH_3), 3.43 (t, 1H, J = 11.1 Hz), 2.18 (s, 3H, CH_3 from acetate), 2.10 (s, 3H, CH_3 from acetate), 2.04 (s, 3H, CH_3 from acetate), 2.03 (s, 3H, CH_3 from acetate), 2.01 (s, 3H, CH_3 from acetate), 1.92 (s, 3H, CH_3 from acetate), 1.69 (s, 3H, CH_3 from acetate).

^{19}F NMR (376 MHz, $CDCl_3$): δ (ppm): −253.7(t,d, J = 47.1 Hz and 27.7 Hz).

^{13}C NMR (75 MHz, $CDCl_3$): δ (ppm): 170.8–169.0, 166.0, 165.5, 133.7, 133.5, 130.1, 129.8, 128.7, 128.6, 97.6, 96.0, 83.4, 82.7 (d, $J_{C,F}$ = 175.6 Hz), 73.1–72.9, 72.2, 70.1–69.3, 68.7, 68.0, 62.9, 61.5, 43.4 (d, $J_{C,F}$ = 6.9 Hz), 21.0–20.8, 20.2.

HRMS (ESI) m/z found: 1039.29124, calculated: 1039.29116 for $C_{47}H_{56}FNaO_{23}S$ $[M + H]^+$.

Methyl α-D-glucopyranosyl-(1–4)-α-D-glucopyranosyl-(1–4)-4-thio-6-deoxy-6-fluoro-α-D-glucopyranoside-MFTMT (6). To a stirred solution of fluorinated maltotriose **5** (0.25 g, 0.24 mmol) in anhydrous methanol (10 mL) was added $NaOCH_3$ (5.4 M, 0.054 mL) and the resulting mixture was stirred under an argon atmosphere overnight. The reaction mixture was neutralized with Amberlite IRN 77 (H^+) (3 g stirred in methanol : $CHCl_3$: water; 25 : 65 : 4). The mixture was filtered, and the filtrate evaporated to dryness under the reduced pressure.

The residue was purified by flash column chromatography on silica gel (CH_3OH : CH_2Cl_2 : H_2O; 27/69/4 to 51/46/3) to afford **6** as white solid (65 mg, 51%).

^{13}C NMR (75 MHz, D_2O): δ (ppm): 100.4, 100.1, 86.4, 83.8 (d, $J_{C,F} = 168.7$ Hz), 77.4, 74.4, 73.5, 73.4, 73.3, 72.6, 72.3, 72.0, 71.4, 70.3 (d, $J_{C,F} = 17.3$ Hz), 69.9, 61.0, 60.8, 55.8, 46.0.

^{19}F NMR (376 MHz, D_2O): δ (ppm) −237.4. t,d, $J = 47.1$ Hz and 28.3 Hz. KF as an internal standard for ^{19}F NMR.

HRMS(ESI) *m*/*z* found: 559.14673, calculated: 539.14817 for $C_{19}H_{33}O_{14}FNa^{32}S$ $[M + Na]^+$.

Methyl 2,3,4,6-tetra-*O*-acetyl-α-D-glucopyranosyl-(1–4)-*O*-(2,3,6-tri-*O*-acetyl-α-D-glucopyranosyl)-(1–4)-2,3-di-*O*-benzoyl-4-thio-6-*O*-trityl-α-D-glucopyranoside (8). To a stirred solution of 2,3,6-tri-*O*-acetyl-*S*-acetyl-(2,3,4,6-tetra-*O*-acetyl-*S*-acetyl-1-thio-α-D-glucopyranosyl)-α-D-glucopyranose[39] **4** (0.44 g, 0.63 mmol) in anhydrous MeOH (12 mL) cooled to −20 °C under an argon atmosphere was added $NaSCH_3$ (0.05 g, 0.63 mmol) and the reaction mixture was stirred at −20 °C for 3 h under argon.

The reaction mixture was neutralized to pH = 7 with 1 N HCl and extracted with EtOAc (50 mL). The EtOAc phase was washed with water (10 mL × 3), dried over Na_2SO_4, filtered, and evaporated to dryness under reduced pressure. A solution of trityl triflate **7** (0.54, 0.63 mmol) in DMF (20 mL) and NEt_3 (0.19 mL) was added to the thiol residue, and the resulting reaction mixture was stirred at 0 °C for 1 h and room temperature for 48 h under argon. EtOAc (100 mL) was added to the reaction mixture, and the EtOAc solution was washed with water (15 mL × 3) and brine (30 mL), dried over Na_2SO_4, filtered, and evaporated to dryness under reduced pressure. The residue was purified by flash column chromatography on silica gel (EtOAc/hexane = 1 : 1) to afford **8** as a colorless glassy solid (0.13 g, 12%).

^{1}H NMR (300 MHz, $CDCl_3$): δ (ppm): 7.90 (m, 4H, ArH), 7.58–7.29 (m, 21H, ArH), 5.98 (t, 1H, $J = 10.4$ Hz), 5.50–5.44 (m, 2H), 5.35 (d, 1H, $J = 4.2$ Hz), 5.24 (d, 1H, $J = 3.5$ Hz), 5.15–5.03 (m, 3H), 4.90 (dd, 1H, $J = 4.2$ and 10.4 Hz), 4.66 (dd, 1H, $J = 6.2$ and 10.4 Hz) 4.27 (dd, 1H, $J = 3.5$ and 12.5 Hz), 4.04–43.68 (m, 8H), 3.54 (s, 3H, OCH_3), 3.51–3.43 (M, 1H), 2.97 (t, 1H, $J = 10.4$ Hz), 2.11 (s, 9H, CH_3 from acetate), 2.03 (s, 3H, CH_3 from acetate), 1.98 (s, 3H, CH_3 from acetate), 1.90 (s, 3H, CH_3 from acetate), 1.64 (s, 3H, CH_3 from acetate).

^{13}C NMR (75 MHz, $CDCl_3$): δ (ppm): 170.79, 170.51, 170.06, 169.70, 169.61, 169.29, 166.11, 165.43, 144.16, 133.55, 133.49, 130.09, 129.82, 129.29, 129.22, 128.91, 128.62, 128.55, 128.25, 127.43, 96.86, 95.86, 87.40, 82.65, 73.74, 73.45, 72.41, 72.10, 70.36, 69.91, 69.54, 68.77, 68.48, 68.18, 65.03, 62.46, 61.46, 55.41, 44.79, 20.92, 20.84.

HRMS (ESI) *m*/*z* found: 1279.40261, calculated: 1279.40505 for $C_{66}H_{71}O_{24}S$ $[M + H]^+$.

Methyl 2,3,4,6-tetra-*O*-acetyl-α-D-glucopyranosyl-(1–4)-*O*-(2,3,6-tri-*O*-acetyl-α-D-glucopyranosyl)-(1–4)-2,3-di-*O*-benzoyl-4-thio-α-D-glucopyranoside (9). A solution of trityl **8** (0.11 g, 0.09 mmol) in 80% HOAc (10 mL) was stirred at 60 °C for 3 h under argon. The reaction was cooled to room temperature and neutralized to pH = 7 by adding saturated $NaHCO_3$. The resulting mixture was extracted with CH_2Cl_2 (50 mL). The organic phase was dried over anhydrous Na_2SO_4, filtered, and evaporated to dryness under reduced pressure. The residue was purified by flash column chromatography on silica gel (EtOAc/heptane = 1 : 1) to afford **9** as a white powder (79 mg, 89%).

^{1}H NMR (300 MHz, $CDCl_3$): δ (ppm): 7.96–7.90 (m, 4H, ArH), 7.54–7.46 (m, 2H, ArH), 7.40–7.32 (m, 4H, ArH), 6.04 (t, 1H, $J = 10.4$ Hz), 5.62 (d, 1H, $J = 5.6$ Hz), 5.40–5.30 (m, 2H), 5.20–5.04 (m, 4H), 4.87 (dd, 1H, $J = 4.2$ and 10.4 Hz), 4.75 (dd, 1H, $J = 5.6$ and 9.4 Hz), 4.56 (d, 1H, $J = 9.7$ Hz), 4.28–3.83 (m, 9H), 3.47 (t, 1H, $J = 11.1$ Hz), 3.42 (s, 3H, OCH_3), 2.33–2.28 (m, 1H), 2.19 (s, 3H, CH_3 from acetate), 2.10 (s, 3H, CH_3 from acetate), 2.04 (s, 6H, CH_3 from acetate), 2.01 (s, 3H, CH_3 from acetate), 1.93 (s, 3H, CH_3 from acetate), 1.70 (s, 3H, CH_3 from acetate).

^{13}C NMR (75 MHz, $CDCl_3$): δ (ppm): 170.80, 170.76, 170.19, 169.65, 169.44, 166.08, 165.48, 133.58, 133.51, 130.06, 129.82, 129.33, 129.17, 128.68, 128.56, 97.50, 96.07, 83.77, 73.37, 73.28, 72.88, 72.03, 70.93, 70.07, 69.87, 69.54, 69.39, 68.67, 68.12, 63.14, 62.20, 61.62, 55.80, 44.71, 21.06, 20.96, 20.89, 20.80, 20.16.

HRMS (ESI) *m*/*z* found: 1037.29419, calculated: 1037.29550 for $C_{47}H_{57}O_{24}S$ $[M + H]^+$.

Methyl 2,3,4,6-tetra-*O*-acetyl-α-D-glucopyranosyl-(1–4)-*O*-(2,3,6-tri-*O*-acetyl-α-D-glucopyranosyl)-(1–4)-2,3-di-*O*-benzoyl-4-thio-6-*O*-brosyl-α-D-glucopyranoside (10). A stirred solution of thiomaltotriose **9** (70 mg, 0.07 mmol) and 4-bromobenzenesulfonyl chloride **2** (106 mg, 0.45 mmol) in CH_2Cl_2 (50 mL) were added DMAP (trace) and NEt_3 (62 μL, 0.45 mmol). The reaction mixture was stirred at room temperature for 24 h under argon and the solvent was removed under reduced pressure. The residue was dissolved in CH_2Cl_2 (20 mL) and washed with water (2 × 5 mL) and brine (5 mL). The organic phase was dried over Na_2SO_4, filtered, and evaporated to dryness under reduced pressure. The residue was purified by flash column chromatography on silica gel (EtOAc/hexanes = 1/1) to afford brosylate–thiomaltotriose **10** as a white solid (54.0 mg, 65%).

^{1}H NMR (300 MHz, $CDCl_3$): δ (ppm): 7.92–7.87 (m, 6H, ArH), 7.79–7.75 (m, 2H, ArH), 7.53–7.45 (m, 2H, ArH), 7.39–7.30 (m, 4H, ArH), 5.95 (t, 1H, $J = 10.4$ Hz), 5.59 (d, 1H, $J = 5.6$ Hz), 5.40–5.33 (m, 2H), 5.17–5.06 (m, 2H), 4.97 (d, 4.87 $J = 3.5$ Hz), 4.90–4.84 (m, 2H), 4.74 (dd, 1H, $J = 5.6$ and 9.8 Hz), 4.71–4.55 (m, 3H), 4.08–3.87 (m, 4H), 3.32 (s, 3H, OCH_3), 3.16 (t, 1H, $J = 11.1$ Hz), 2.17 (s, 3H, CH_3 from acetate), 2.10 (s, 3H, CH_3 from acetate), 2.04 (s, 6H, CH_3 from acetate), 2.00 (s, 3H, CH_3 from acetate), 1.93 (s, 3H, CH_3 from acetate), 1.69 (s, 3H, CH_3 from acetate).

^{13}C NMR (75 MHz, $CDCl_3$): δ (ppm): 170.81, 170.76, 170.55, 170.08, 169.70, 169.66, 169.45, 165.92, 165.38, 135.31, 133.71, 133.59, 132.80, 130.05, 129.87, 129.48, 129.11, 128.98, 128.72, 128.58, 97.16, 96.11, 83.45, 73.12, 72.98, 72.48, 71.92, 70.26, 70.00, 69.84, 69.59, 69.55, 68.71, 68.59, 67.98, 62.74, 61.50, 55.99, 44.91, 21.13, 20.92, 20.84, 20.22.

HRMS (ESI) *m*/*z* found: 1255.19745, calculated: 1255.19921 for $C_{53}H_{60}BrO_{26}S_2$ $[M + H]^+$.

Methyl 2,3,4,6-tetra-*O*-acetyl-α-D-glucopyranosyl-(1–4)-2,3-di-*O*-benzoyl-4-thio-6-deoxy-6-fluoro-α-D-glucopyranoside (12). To a stirred solution of 2,3,4,6-tetra-*O*-acetyl-1-*S*-acetyl-1-thio-α-D-glucopyranose **11** (0.1989 g, 0.49 mmol) in anhydrous MeOH (5 mL) cooled to −20 °C under an argon atmosphere was added

$NaSCH_3$ (0.0361 g, 0.49 mmol) and the reaction mixture was stirred at −20 °C for 3 h under an argon atmosphere. The reaction mixture was neutralized to pH = 7 with 1 N HCl and extracted with EtOAC (60 mL). The organic phase was washed with water (20 mL × 3), dried over Na_2SO_4, filtered, and evaporated to dryness under reduced pressure. A solution of triflate 3 (0.38, 0.71 mmol) in DMF (17 mL) and NEt_3 (0.4 mL) was added to the thiol residue, and the resulting reaction mixture was stirred at 0 °C for 1 h and then at ambient temperature under argon overnight. The solvent of the resulting crude product mixture was evaporated under reduced pressure. The resulting mixture was dissolved in EtOAc (60 mL), washed with water (5 mL × 5), dried over Na_2SO_4, filtered, and evaporated to dryness under reduced pressure. The residue was purified using flash column chromatography on silica gel (EtOAc/hexane = 1 : 3) to afford **12** as a colorless foamy solid (0.2165 g, 59%).

^{1}H NMR (300 MHz, $CDCl_3$): δ (ppm): 7.96–7.88 (m, 4H, ArH), 7.56–7.45 (m, 2H, ArH), 7.41–7.31 (m, 4H, ArH), 6.05 (t, 1H, J = 10.5 Hz), 5.79 (d, 1H, J = 6.3 Hz), 5.26–5.20 (m, 2H), 5.12–4.86 (m, 4H), 4.73 (dd, 1H, J = 9.9 and 48.9 Hz), 4.79–4.69 (m, 2H), 4.41 (dd, 1H, J = 3.8 Hz and 12.3 Hz), 4.30–4.25 (m, 1H), 4.11 (dd, 1H, J = 2.1 and 12.3 Hz), 3.97 (dd, 1H, J = 10.5 and 28.5 Hz), 3.43 (s, 3H, OCH_3), 3.43 (t, 1H, J = 11.1 Hz), 2.12 (s, 3H, CH_3 from acetate), 2.02 (s, 3H, CH_3 from acetate), 1.94 (s, 3H, CH_3 from acetate), 1.71 (s, 3H, CH_3 from acetate).

^{19}F NMR (376 MHz, $CDCl_3$): δ (ppm) −253.79 (t,d, J = 47.0 and 28.2 Hz).

^{13}C NMR (150 MHz, $CDCl_3$): δ (ppm) 170.7, 169.9, 169.4, 169.0, 165.8, 165.4, 133.5, 133.3, 129.9, 129.0, 128.9, 128.5, 128.4, 97.4, 83.3, 82.4 (d, $J_{C,F}$ = 175.6 Hz), 73.0, 72.8, 70.1, 69.5, 69.4 (d, $J_{C,F}$ = 18.6 Hz), 68.7, 68.0, 61.4, 55.8, 42.7 (d, $J_{C,F}$ = 6.8 Hz), 20.7, 20.6, 20.0.

HRMS (ESI) m/z found: 773.18867, calculated: 773.18859 for $C_{35}H_{39}O_{15}F_{23}Na^{32}S$ $[M + Na]^+$.

Methyl α-D-glucopyranosyl-(1–4)-4-thio-6-deoxy-6-fluoro-α-D-glucopyranoside (13). To a stirred solution of fluorinated maltose **12** (0.20 g, 0.27 mmol) in anhydrous methanol (6 mL) was added $NaOCH_3$ in methanol (25 wt%, 0.13 mL) and the resulting mixture was stirred under an argon atmosphere overnight at ambient temperature. The reaction mixture was neutralized with Amberlite IRN 77 (H^+) (3 g). The mixture was filtered, and the filtrate was evaporated to dryness under reduced pressure. The residue was purified by flash column chromatography on silica gel ($CH_3OH : CH_2Cl_2 : H_2O$ = 27/69/4 to 51/46/3) to afford **13** as a white solid (98.9 mg, 99%).

^{13}C NMR (150 MHz, D_2O): δ (ppm): 102.3, 88.9, 86.1 (d, $J_{C,F}$ = 169.0 Hz), 76.2, 75.7, 75.6, 74.9, 73.9, 72.4 (d, $J_{C,F}$ = 17.6 Hz), 72.2, 63.1, 58.1, 48.4 (d, $J_{C,F}$ = 5.7 Hz).

^{19}F NMR (376 MHz, D_2O): δ (ppm): −237.3 (t,d, J = 47.1 and 28.4 Hz).

HRMS (ESI) m/z found: 397.09437, calculated: 397.0939 for $C_{13}H_{23}O_9FNa^{32}S$ $[M + Na]^+$.

Radiochemistry

[^{18}F]MFTMT ([^{18}F]6). The automated synthesis of [^{18}F]MFTMT was carried out in a TRACERlab FX2 N. The radiosynthesis of [^{18}F]MFTMT was accomplished *via* the following procedure: (1) [^{18}F] fluorination of precursor **10**; (2) basic hydrolysis of [^{18}F]**14**; (3) HPLC purification of [^{18}F]MFTMT; and (4) formulation. Prior to the start of synthesis of [^{18}F]MFTMT, appropriate reagent solutions were loaded into four reagent vials on the FX2 N Pro module. Vial 1 was used for the elution of [^{18}F]-fluoride from the QMA cartridge. Vial 3 was used for precursor; vials 4 and 5 were used for basic hydrolysis and neutralization, respectively prior to HPLC purification. Vials 2 and 6 were empty. Vial 1 was added with fresh 11 mg K_{222} in 1.0 mL methanol, 0.8 mg K_2CO_3 in 0.2 mL water, Vial 3 was added with the brosylate precursor **10** (4.5 mg) in dry acetonitrile (1.0 mL); Vial 4 was added with 21 wt% NaOEt in ethanol (0.3 mL) and USP ethanol (0.7 mL) and Vial 5 was added with 1 N HCl (0.8 mL) and citrate buffer (200 mM, 2 mL). [^{18}F]-Fluoride, 1.56 Ci of no-carrier-added [^{18}F]HF (60 μA, 60 min bombardment, theoretical specific activity of 1.7 Ci per nmole), produced on a Siemens RDS 111 cyclotron was adsorbed on QMA cartridge. The [^{18}F]-fluoride was eluted from the QMA cartridge with 11 mg K_{222} in 1.0 mL methanol and 0.8 mg K_2CO_3 in 0.2 mL water into Reactor 1. The Reactor 1 temperature was raised up to 65 °C with helium flow and vacuum for 3 min. The temperature is then raised to 95 °C with vacuum and helium flow for another 3.5 min. Finally, for another 3.5 min at 95 °C vacuum applied for solvent evaporation to dryness. Brosylate precursor **10** (4.5 mg, 3.6 μmol) in 1.0 mL of dry acetonitrile was added from Vial 3. The radiofluorination process was performed at 100 °C for 20 min. Following radiofluorination the Reactor 1 temperature was lowered to 50 °C and solvent evaporation was performed under vacuum with helium flow for 3 min to dryness. The basic hydrolysis process was performed by adding 21 wt% NaOEt in ethanol (0.3 mL) and USP ethanol (0.7 mL) from Vial 4 followed by heating at 100 °C for 10 min and 80 °C for 5 min. The hydrolysis at 80 °C was performed under helium gas flow. After basic hydrolysis the Reactor 1 temperature was lowered to 40 °C and the reaction mixture was neutralized by adding 1 N HCl (0.8 mL) and citrate buffer (200 mM, 2 mL) from Vial 5. The neutralized solution was injected onto a Waters Atlantis T3, 5 μm, 19 mm × 100 mm HPLC column. The HPLC purification was done at 6 mL min^{-1} using 6% EtOH–water as eluent. The radioactive peak of [^{18}F]MFTMT was collected at 7.5–8.1 min into a flask. Finally, the product in 4 mL 6% EtOH–water was sterilized by passing through a Millex®-GS sterile filter (0.22 μm) into an aseptically prepared dose vial. A total of 188 mCi of [^{18}F]MFTMT was obtained from 1560 mCi of ^{18}F-fluoride in a synthesis time of 80 min. The purified final product [^{18}F]MFTMT was diluted in a saline solution (pH = 6) and used for PET imaging studies. [^{18}F]MFTMT was identified by co-injection of [^{18}F]MFTMT and non-radiolabelled [^{19}F]MFTMT **6** onto a Waters Atlantis T3, 3 μm, 4.6 mm × 150 mm HPLC column which was eluted using 3% ethanol–water as eluent over 20 min at a flow rate of 1 mL min^{-1} (approximate retention time of [^{18}F]MFTMT is 10.0–11.0 min).

Biological analyses

Bacteria uptake assays. To evaluate the uptake of [^{18}F]MFTMT by bacteria and mammalian cells, we used wild-type *Escherichia coli* (*E. coli*, ATCC33456), wild-type *Staphylococcus*

aureus (*S. aureus*, ATCC25923), LamB mutant *E. coli* (LamB KO *E. coli*, JW3996-1), *Staphylococcus epidermidis* (NRS101), *Pseudomonas aeruginosa* (ATCC 27853), *Enterococcus faecalis* (ATCC 29212), *Streptococcus sanguinis* (ATCC 10556) and CHO-K1 cells (ATCC CCL61). In LamB KO *E. coli*, the deletion of the lamB gene from the genomic sequence results in the inability to internalize maltodextrins *via* maltoporins. To evaluate the affinity to [^{18}F]MFTMT, *E. coli*, *S. aureus* and LamB KO *E. coli* were cultured in Luria–Bertani broth (LB broth, Research Products International), and cultures in the exponential stage were adjusted to an optical density at 600 nm (OD600) of 0.3, corresponding to a concentration of 1×10^8 CFU mL^{-1}. Subsequently, the bacterial suspension was aliquoted into 24-well plates, and [^{18}F]MFTMT was loaded at final concentrations of 5, 10, 15, and 20 μCi mL^{-1} ($N = 3$ for each concentration). The bacteria were incubated at 37 °C for 1 h. After incubation, 200 μL of bacterial suspension was aliquoted onto 0.22 μm centrifuge filter cartridges (F2517-1, Thermo Scientific). The filter cartridges were centrifuged at 3000×*g* for 1 min and transferred to new tubes. Next, 600 μL of PBS was added, followed by centrifugation at 3000×*g* for 1 min to wash the bacteria on the filter. The filter cartridges were then placed in new tubes and centrifuged at 3000×*g* for 1 min to remove any remaining liquid. Finally, the filter cartridges were used to measure the radioactivity associated with the bacteria on the filter.

CHO-K1 cells were cultured in Ham's F-12 Nutrient Mix medium (Thermo-Fisher Scientific) containing 10% fetal bovine serum (Sigma-Aldrich) and penicillin/streptomycin (Sigma-Aldrich). Cells were seeded onto 6-well plates at a density of 10 000 cells per well one day before the experiment. The cells were then loaded with [^{18}F]MFTMT at final concentrations of 5, 10, 15, and 20 μCi mL^{-1} and incubated at 37 °C for 1 h ($N = 3$ for each concentration). Subsequently, the cells were washed three times with 2 mL of PBS per well. After that, the cells were detached from the plates using cell scrapers and suspended in 0.5 mL of PBS. The resulting cell suspension was transferred to 1.5 mL tubes for their radioactivity assessment.

To evaluate the uptake of serum-treated [^{18}F]MFTMT, [^{18}F]MFTMT was incubated with a 1/10 volume of rat serum at 37 °C for 1 h, followed by filtration with a molecular filter (PALL 0.45 μm PTFE ACRODISC CR 13). The resulting serum-treated [^{18}F]MFTMT solution was then analyzed for radioactivity. Bacteria and CHO-K1 cells were prepared as previously described, and the serum-treated [^{18}F]MFTMT was added at final concentrations of 1, 5, 10, and 15 μCi mL^{-1} and incubated at 37 °C for 1 h ($N = 3$ for each concentration). After incubation, bacteria and cells were processed as described earlier.

In addition to *S. aureus* and *E. coli*, uptake of [^{18}F]MFTMT and [^{18}F]MFTM by *Pseudomonas aeruginosa*, *Staphylococcus epidermidis*, *Enterococcus faecalis*, *Streptococcus sanguinis* were also evaluated. *Enterococcus faecalis* and *Streptococcus sanguinis* were cultured in Brain Heart Infusion Broth (BHI broth, Research Products International) and in aerobic condition. Other bacteria were cultured in LB broth and aerobic condition. [^{18}F]MFTM was generated by digesting 1 mCi mL^{-1} of [^{18}F]MFTMT by 50 units per mL of α-glucosidase (G5003, Sigma-Aldrich) at 3737 °C for 1 h, then, the enzyme, α-glucosidase was removed using 10 kD molecular filters (Amicon Ultra-0.5 Centrifugal Filter Unit, Millipore). As described above, the bacteria were adjusted to the OD600 of 0.3 (concentration of 1×10^8 CFU mL^{-1}), and incubated with 20 μCi mL^{-1} of [^{18}F]MFTMT or [^{18}F]MFTM at 37 °C for 1 h ($N = 3$). Then, 200 μL of bacterial suspension was aliquoted onto the 0.22 μm centrifuge filter cartridges and washed with PBS. The bacterial pellets on the filter cartridges were used to evaluate the radioactivity.

The remaining radioactivity associated with bacteria or CHO-K1 cells was measured using a gamma counter (Cobra II gamma counter, Packard). Radioactivity levels were quantified using standards ranging from 0.0005 to 0.01 μCi ($N = 2$ for each standard concentration).

In vivo PET imaging

Rat skin-pocket infection model. The animal experiment protocols were approved by Emory University IACUC (PROTO201700652). To investigate whether [^{18}F]MFTMT accumulates bacteria *in vivo*, we utilized a rat skin-pocket-infection model that we have previously established.[18] Briefly, 8-week-old male rats were obtained from Charles River Laboratories (South Carolina, USA) and small surgical-grade metal mock-ups resembling implantable cardiac devices were surgically implanted on their backs. On postoperative day (POD) 4, the rats were randomly divided into four groups. The infection groups were inoculated with either *E. coli* or *S. aureus*, each containing 1×10^9 CFU, in the skin pocket surrounding the mock-up (referred to as the *E. coli* and *S. aureus* groups, respectively). Additionally, some rats were injected with 20 μL of turpentine oil around the mock-ups to induce non-infectious inflammation (classified as the non-infectious inflammation group). Control rats received no additional treatment. On POD6, the rats were subjected to *in vivo* [^{18}F]MFTMT PET imaging ($N = 3$ to 4 for each group). In this rat pocket infection model, the infected lesion contained 2.9×10^8 CFU of bacteria at the time of imaging.[18]

Administration of tracer. Rats were anesthetized using isoflurane gas. Anesthesia was initiated 10 min ahead of imaging experiments, achieved by placing the animal in a cage ventilated with oxygen and 1–2% isoflurane. The body temperature was held at 37 °C using a temperature-controlled warm air convection system. The tracer was administered into the tail vein. The tracer, diluted in 6% EtOH, was mixed with saline to achieve a final volume of 0.4 mL and injected *via* the catheter.

Rat MicroPET-CT studies. After anesthesia, the animal was positioned at the center of the field of view. The rats were injected with 200–250 μCi of [^{18}F]MFTMT in 0.4 mL of isotonic saline-6% EtOH (pH = 6–7). MicroPET-CT imaging data were acquired with a Siemens Inveon PET/CT system (Siemens Medical Solutions, Knoxville, TN, USA). Radioactivity levels in the syringe were measured before and after tracer injection to the tail vein catheter using a Capintec CRC 15R (Capintec Inc, 6 Arrow Road Ramsey, NJ) dose calibrator. Data acquisition was performed for 60 min, starting immediately following tracer injection. After PET imaging, all animals underwent computed tomography (CT) transmission imaging in a position similar to that used for PET.

Animals were euthanized using carbon dioxide following CT. PET emission data were normalized and corrected for the decay of fluorine-18 and detector dead time. Images were reconstructed using an ordered-subset expectation maximization algorithm, with attenuation correction from CT, into fifteen 1-min frames followed by eleven 5-min frames. The image volume consisted of 128 × 128 × 159 voxels, each measuring 0.78 mm × 0.78 mm × 0.80 mm. PET and CT images were co-registered using ASIPro and processed using software written by the authors. Regions-of-interest (ROIs) were placed on the fused PET/CT data including infection pocket. The time–activity curves represent the mean activity in the regions-of-interest over time.

Analysis of PET imaging data. Radioactivity accumulation was evaluated using the summed image for the late time point (27.5 to 60 min) once the change in blood radioactivity had stabilized. ROIs were delineated by tracing the target areas in the transverse section view to assess accumulation around the mock-up area and on the dorsum of the animals, contralateral to the side of the mock-ups, at each time point. The standardized uptake values (SUVs) within the ROIs were used for quantitative assessment. The mean SUV (SUV mean) was calculated as [(total radioactivity in the ROI)/(volume of ROI)]/[(administered radioactivity)/(body weight)], while the maximum SUV (SUV max) was calculated as (highest pixel value in the ROI)/[(administered radioactivity)/(body weight)]. SUV mean and SUV max in the mock-up areas were compared to those in normal skin areas, yielding SUVmean and SUVmax ratios, respectively.[110,111] Blood radioactivity retention was expressed as the ratio to the injected dose (% ID per g tissue), which was calculated as 100 × (radioactivity in 1 gram of tissue)/(injected radioactivity).[17]

Metabolite(s) of [^{18}F]MFTMT

***In vitro* serum stability of [^{18}F]MFTMT.** Rat and human serum stability tests were performed by an adaptation of a previously reported method.[109] Rat serum was purchased from Sigma Aldrich, while human serum was freshly acquired from both female and male donors. [^{18}F]MFTMT, dissolved in a solution of 6% EtOH–water (200 μL; 0.1 mCi, 3.7 MBq), was added to either rat or human serum (2000 μL). The resulting mixtures were aliquot into triplicate 1.5 mL conical tubes in 100 μL portions and then incubated at 37 °C for 5, 15, and 30 min.

Following the designated incubation period, 200 μL of the ice-cold methanol was added to each tube and mixed. Subsequently, the samples were centrifuged at 20 000 relative centrifugal force for 10 min. The supernatants were removed and injected into a Waters Breeze HPLC system equipped with a 5 μL stainless steel injection coil installed and a Waters Atlantis T3, 3 μm, 4.6 mm × 150 mm HPLC column. Elution was achieved using 2% EtOH–water as the eluent over 25 min at a flow rate of 1 mL min^{-1}.

***In vivo* metabolite(s) of [^{18}F]MFTMT.** *In vivo* metabolites of [^{18}F]MFTMT were evaluated using the non-infectious inflammation rat model. The rats were injected with turpentine oil as described above, and after 2 days, the rats were injected with 250 μCi of [^{18}F]MFTMT *via* the tail vein. The rats were sacrificed with an overdose of pentobarbital. The blood, tissue around the mock-ups, the liver, and the kidneys were excited. The tissue and organ samples (approximately 2 g) were added with 1/10 volume of PBS (approximately 200 μL) and were homogenized with a tissue homogenizer. The homogenized samples were centrifuged at 4500×*g* for 30 min to obtain the tissue extract. The coagulated blood was centrifuged at 1500×*g* for 15 min to obtain the serum. The tissue extract and serum were analyzed with a Waters Breeze HPLC system equipped with a 5 μL stainless steel injection coil installed and a Waters Atlantis T3, 3 μm, 4.6 mm × 150 mm HPLC column. Elution was achieved using 2% EtOH–water as the eluent over 25 min at a flow rate of 1 mL min^{-1}.

Immunohistochemistry. The infection, non-infectious inflammation, and control rats were sacrificed at POD 6, coinciding with the time point for PET imaging. Skin samples around the mock-up were collected and fixed in 10% formalin for 48 h. These skin samples were then embedded in paraffin and sliced into 5 μm sections. To assess cells expressing sodium glucose co-transporter1 (SGLT1) and SGLT2, the samples were stained with rabbit anti-SGLT1 antibody (NBP2-20338, Novus, 1 : 100) or rabbit anti-SGLT2 antibody (GTX59872, GeneTex, 1 : 100). Concurrently, to identify fibroblasts, a mouse anti-vimentin antibody (NBP1-97672, Novus, 1 : 100) was used. Following PBS washing, the sections were stained with secondary antibodies: donkey anti-rabbit IgG conjugated with Alexa Fluor 568 (A10042, Invitrogen, 1 : 500) and donkey anti-mouse IgG conjugated with Alexa 488 (A-21202, Invitrogen, 1 : 500). Finally, the sections were sealed with a mounting medium containing 4′,6-diamidino-2-phenylindole (DAPI, VECTASHIELD with DAPI, H-1800). The expression of SGLT1, SGLT2, and vimentin were observed using a confocal microscope (Leica TCS SP5 II).

Quantitative polymerase chain reaction (qPCR). Expression of SGLT1, SGLT2 and β-actin as the internal control in the inflammatory tissue was evaluated by qPCR. The non-infectious inflammation and control rats were sacrificed at POD6. The tissue around the mock-ups was harvested, coinciding with the time point for PET imaging. The samples were immediately frozen with liquid nitrogen. The samples were homogenized in QIAzol Lysis Reagent (Qiagen) and total ribonucleic acid (RNA) was extracted with RNeasy Mini Kit (Qiagen). Complementary deoxyribonucleic acid (cDNA) was synthesized from 4.7 μg of total RNA for 20 μL of reaction using RevertAid First Strand cDNA Synthesis Kit (Thermo-Fisher Scientific). The sequences of primers were as follows: SGLT1 forward: cgtcttcctgctggctattttc, reverse: atgcgctcttctgtgctgttac,[112] SGLT2 forward: ctgaacttggggagcagaag, reverse: cacaagccaa-caccaatgac,[113] and β-actin (PrimeTime qPCR primers Rn.PT.39a.22214838.g, Integrated DNA Technologies) forward: tcactatcggcaatgagcg, reverse: ggcatagaggtctttacggatg. For the qPCR reaction, 1 mL of cDNA, 800 nM of primers (400 nM each forward and revers primer) and 5 μL PowerTrack SYBR Green Master Mix (Thermo-Fisher Scientific) were mixed in total 10 μL of reaction buffer, and the qPCR reaction was conducted per the manufactures instruction using a StepOnePlus Real-Time PCR System (Thermo-Fisher Scientific). The expressions of SGLT1 and SGLT2 were evaluated by the expression relative to β-actin.

Interaction of [^{18}F]MFTMT with SGLTs

Plasmid construction. The mammalian expression vector, pCMV6-A-puro plasmid (PS100025), was obtained from OriGene. Restriction enzymes, ligation enzymes, and T4 polymerase were obtained from New England Biolabs. To modify the muti-cloning site (MCS), the MCS template (gcggacggtgagtactggatgaaccgaggagagatatcgcggccgccaccatggaccgacactcgagagatacgatcagcaagcttccgtgcgtgcgcc) was generated using polymerase chain reaction (PCR) and digested with ScaI and HindIII. The resulting digested template (68 bps) was inserted into the blunted EcoRI to the Hind III site of pCMV6-A-puro. Human SGLT1 (hSGLT1) and SGLT2 (hSGLT2) cDNA clones were obtained from R&D systems (RDC0654 and RDC0557, respectively). The fragments containing the target genes, hSGLT1 or hSGLT2, were extracted using NotI and XhoI digestion and subsequently subcloned into the NotI–XhoI site of pCMV6-A-puro. IRES-mCherry plasmid (a gift from Dr Ellen Rothenberg, Addgene plasmid # 80139; http://n2t.net/addgene:80139; RRID:Addgene_80139)[114] had its EcoRI to XhoI site (1351 base pairs) inserted into pCMV6-A-puro with hSGLT1 and pCMV6-A-puro with hSGLT2 (yielding pCMV6-hSGLT1mCherry and pCMV6-hSGLT2mCherry, respectively). The mCherry gene was amplified by PCR using a forward primer gccgttaacatggtgagcaagggcgaggaggata and a reverse primer ctaagtgaattcttacttgtacagctcgtccatgccgccg and subsequently subcloned using the Zero Blunt TOPO PCR cloning kit (450245, Invitrogen). The mCherry gene, extracted using HpaI and XhoI previously added into the TOPO vector, was then subcloned into the blunted HindIII and the XhoI site (pCMV6-mCherry).

Human SGLT1 and SGLT2 expression in CHO-K1 cells. CHO-K1 cells were cultured and seeded in a 24-well plate at a density of 0.6×10^5 cells per well, as previously described, one day before plasmid transfection. Mammalian expression vectors, pCMV6-hSGLT1, pCMV6-hSGLT2, and pCVM6-mCherry, were transfected using FuGENE HD (Promega) at the ratio of plasmid to FuGENE HD of 1 : 4, following the manufacturer's instructions. The medium was changed one day after the transfection, and the expression of transfected genes was confirmed by observing mCherry expression using a fluorescent microscope (Olympus IX71). Cells were selected with puromycin (10 μg mL^{-1}, Santa Cruz) for 3 weeks and seeded in a 96-well plate at a density of 1 cell per well. The stable expression of hSGLT1 or hSGLT2 was confirmed by assessing the uptake of 1-NBDG (0.1 mM, V41383, InvivoChem), a specific substrate for SGLT1 and SGLT2.[60] CHO-K1 cells with the highest uptake of 1-NBDG were designated as CHO-K1-hSGLT1 and CHO-K1-hSGLT2. Among the cells transfected with pCVM6-mCherry, those exhibiting the highest mCherry expression were selected as CHO-K1-control.

Interaction of [^{18}F]MFTMT and [^{18}F]MFTM with SGLTs. The CHO-K1-hSGLT1, CHO-K1-hSGLT2, and CHO-K1-control cells were seeded in 6-well plates at a density of 12 000 cells per well one day before the experiment. The cells were then loaded with [^{18}F]MFTMT and [^{18}F]MFTM at a final concentration of 20 μCi mL^{-1} and incubated at 37 °C for 1 h ($N = 3$). Subsequently, the cells were washed, and the remaining radioactivity in the cells was evaluated using the method described in the *in vitro* uptake study. To confirm the specificity of the interactions with SGLT1 and/or SGLT2, some CHO-K1 hSGLT1 and COH-K1 SGLT2 cells were treated with mizagliflozin (MedChemExpress), a specific SGJT1 inhibitor and dapagliflozin (Combi-Blocks), a specific SGLT2 inhibitor at final concentration of 1 μM for 30 min.[104,105,115–117] Then, the cells were loaded with [^{18}F]MFTMT and [^{18}F]MFTM at a final concentration of 20 μCi mL^{-1} ($N = 3$).

Statistical evaluation

Statistical analysis was conducted using Prism statistical software (Version 5.01). The Student's *t*-test was utilized to compare two groups, while a one-way analysis of variance was employed with Tukey's multiple comparison tests. All data are presented as mean ± standard error, with a significance level of $p < 0.05$ considered statistically significant.

Conclusions

In this study, we synthesized [^{18}F]MFTMT and assessed its serum stability, *in vitro* uptake, and *in vivo* distribution and metabolism. While the thio-glycosyl bond resisted enzymatic digestion, [^{18}F]MFTMT and its metabolite, [^{18}F]MFTM, reduced the affinity for *E. coli* and other pathogenic bacteria other than *S. aureus*, and thio-glycosyl bond and/or 6-deoxy-6-fluoro-modification prolonged blood retention of radioactivity. *In vivo* imaging revealed that radioactivity derived from [^{18}F]MFTMT accumulated not only in *S. aureus*-infected lesions but also in inflammatory tissue. We further found that [^{18}F]MFTM is the only radioactive metabolite *in vivo*, and increased SGLT1 expression in the inflammatory tissue likely contributed to non-specific [^{18}F]MFTMT and [^{18}F]MFTM accumulation in PET imaging. In addition, delayed excretion of [^{18}F]MFTMT and/or its metabolites might further increase radioactivity accumulation in inflammatory tissue.

Our findings suggest that for bacteria-specific probes for PET imaging, maltotetraose and/or a longer maltodextrin backbone may reduce accumulation in mammalian cells caused by SGLT1 and may be a key for specificity to bacteria. Furthermore, a thio-glycosyl bond may reduce the affinity to maltodextrin transporter and PTS and other approaches such as employing a nitrogen-glycosyl bond may satisfy both stability against enzymatic digestion and specificity for bacteria. Moreover, the optimal position to derivatize the imaging molecule might be different depending on the species of bacteria. Based on these findings, future studies will need to investigate the structure and characteristics of maltodextrin transporters of pathogenic bacteria. These studies will lead to the development of next generation maltodextrin-based imaging probes with nitrogen-glycosyl bond making them resistant to enzymatic digestion while maintaining bacterial selectivity and even bacterial species specificity.

Abbreviations

1-NBDG	1(*N*-(7-Nitrobenz-2-oxa-1,3-diazol-4-yl) amino)-1-deoxy-D-glucose
% ID per g tissue	Ratio relative to the injection dose per gram

BHI broth	Brain heart infusion broth
CFU	colony-forming units
CT	Computed tomography
DAPI	4′,6-Diamidino-2-phenylindole
E. coli	*Escherichia coli*
E. faecalis	*Enterococcus faecalis*
EIIC	Enzyme IIC component
EtOH	Ethanol
[^{18}F]FDG	2-Deoxy-2-[^{18}F]fluoro-D-glucose
GLUT	Glucose transporter
HPLC	High-performance liquid chromatography
LB broth	Luria–Bertani broth
MFTM	Methyl 6-deoxy-6-fluoro-4-thio-α-D-maltoside
MFTMT	Methyl 6-deoxy-6-fluoro-4-thio-α-D-maltotrioside
MHF	Fluoro-maltohexaose
MRI	Magnetic resonance imaging
NaOEt	Sodium ethoxide
NEt3	Triethylamine
NMR	Nuclear magnetic resonance
P. aeruginosa	*Pseudomonas aeruginosa*
PBS	Phosphate-buffered saline
PET	Positron emission tomography
POD	Postoperative day
PTS	Phosphotransferase system
RCY	Decay-corrected radiochemical yield
ROI	Region of interest
S. aureus	*Staphylococcus aureus*
S. epidermidis	*Staphylococcus epidermis*
SDS-PAGE	Sodium dodecyl-sulfate polyacrylamide gel electrophoresis
SGLT	Sodium glucose co-transporter
S. sanguinis	*Streptococcus sanguinis*
SUV	Standardized uptake value
TLC	Thin-layer chromatography

Data availability

The data supporting this article has been included as part of the ESI.†

Author contributions

Kiyoko Takemiya: investigation, formal analysis, methodology, visualization, writing – original draft, writing – review & editing, and graphical abstract. Wonewoo Seo: investigation, formal analysis, methodology, and writing – original draft. Ronald J. Voll: investigation, formal analysis. Sheng Zhao: investigation. Giji Joseph: investigation. Shelly Wang: investigation. Fanxing Zeng: investigation. Jonathon A Nye: investigation. Niren Murthy: conceptualization, writing – review & editing, funding acquisition. W. Robert Taylor: conceptualization, writing – review & editing, funding acquisition. Mark M. Goodman: conceptualization, methodology, visualization, writing – original draft, writing – review & editing, funding acquisition, and graphical abstract.

Conflicts of interest

Mark Goodman is the principal investigator, a sponsor of this study. The terms of this arrangement have been reviewed and approved by Emory University in accordance with Emory University Policy 7.7, Policy for Investigators Holding a Financial Interest in Research. Kiyoko Takemiya, W. Robert Taylor, Niren Murthy, and Mark M. Goodman have equity interest in Microbial Medical, Inc., which is related to this study. Wonewoo Seo, Ronald J. Voll, Sheng Zhao, Giji Joseph, Shelly Wang, Fanxing Zeng, and Jonathon A. Nye have no conflict of interests.

Acknowledgements

This study has been funded in part with Federal funds from the National Institute of Biomedical Imaging and Bioengineering, National Institutes of Health, Department of Health and Human Services, under Grants No. NIH R01 EB029320 and NIH R01 EB020008. This study is supported by gifts from the True Vine Foundation and an anonymous donor. The authors thank Dr Jaekeun Park for his contribution in the micro-PET studies and Ron Crowe, BCNP, and the radiopharmacy at the Emory University Center for Systems Imaging for production of [^{18}F] fluoride.

Notes and references

1 A. J. Greenspon, J. D. Patel, E. Lau, J. A. Ochoa, D. R. Frisch, R. T. Ho, B. B. Pavri and S. M. Kurtz, *J. Am. Coll. Cardiol.*, 2011, **58**, 1001–1006.
2 B. L. Wilkoff, G. Boriani, S. Mittal, J. E. Poole, C. Kennergren, G. R. Corey, J. C. Love, R. Augostini, S. Faerestrand, S. S. Wiggins, J. S. Healey, R. Holbrook, J. D. Lande, D. R. Lexcen, S. Willey, K. G. Tarakji and W.-I. Investigators, *Circ.: Arrhythmia Electrophysiol.*, 2020, **13**, e008280.
3 R. Sanghavi, N. Ravikumar, V. Sarodaya, M. Haq, M. Sherif and A. Harky, *Future Cardiol.*, 2022, **18**(11), 891–899.
4 K. G. Tarakji and B. L. Wilkoff, *Expet Rev. Cardiovasc. Ther.*, 2013, **11**, 607–616.
5 A. Roque, J. Francisco-Pascual, J. F. Andres-Cordon, N. Fernandez-Hidalgo, J. R. Herance, H. Cuellar-Calabria, S. Aguade-Bruix and M. N. Pizzi, *J. Nucl. Cardiol.*, 2023, **30**, 2846–2849.
6 D. C. DeSimone and M. R. Sohail, *J. Clin. Microbiol.*, 2018, **56**(7), e01683.
7 B. L. Wilkoff, G. Boriani, S. Mittal, J. E. Poole, C. Kennergren, G. R. Corey, A. D. Krahn, E. J. Schloss, J. L. Gallastegui, R. A. Pickett, R. F. Evonich, S. F. Roark, D. M. Sorrentino, D. P. Sholevar, E. M. Cronin, B. J. Berman, D. W. Riggio, H. H. Khan, M. T. Silver, J. Collier, Z. Eldadah, R. Holbrook, J. D. Lande, D. R. Lexcen, S. Seshadri and K. G. Tarakji, *Circ.:Arrhythmia Electrophysiol.*, 2020, **13**, e008503.
8 T. W. van der Vaart, P. M. M. Bossuyt, D. T. Durack, L. M. Baddour, A. S. Bayer, E. Durante-Mangoni, T. L. Holland, A. W. Karchmer, J. M. Miro, P. Moreillon,

M. Rasmussen, C. Selton-Suty, V. G. Fowler Jr and J. T. M. van der Meer, *Clin. Infect. Dis.*, 2024, **78**(4), 922–929.
9 V. G. Fowler, D. T. Durack, C. Selton-Suty, E. Athan, A. S. Bayer, A. L. Chamis, A. Dahl, L. DiBernardo, E. Durante-Mangoni, X. Duval, C. Q. Fortes, E. Fosbol, M. M. Hannan, B. Hasse, B. Hoen, A. W. Karchmer, C. A. Mestres, C. A. Petti, M. N. Pizzi, S. D. Preston, A. Roque, F. Vandenesch, J. T. M. van der Meer, T. W. van der Vaart and J. M. Miro, *Clin. Infect. Dis.*, 2023, **77**, 518–526.
10 A. S. Dababneh and M. R. Sohail, *Cleve. Clin. J. Med.*, 2011, **78**, 529–537.
11 K. G. Tarakji, E. J. Chan, D. J. Cantillon, A. L. Doonan, T. Hu, S. Schmitt, T. G. Fraser, A. Kim, S. M. Gordon and B. L. Wilkoff, *Heart Rhythm*, 2010, **7**, 1043–1047.
12 M. Nataloni, M. Pergolini, G. Rescigno and R. Mocchegiani, *J. Cardiovasc. Med.*, 2010, **11**, 869–883.
13 R. Margey, H. McCann, G. Blake, E. Keelan, J. Galvin, M. Lynch, N. Mahon, D. Sugrue and J. O'Neill, *Europace*, 2010, **12**, 64–70.
14 B. L. Wilkoff, *Heart Rhythm*, 2007, **4**, 1467–1470.
15 M. Unberath and A. Maier, Medical imaging modalities, in *Medical Image Analysis*, ed. A. F. Frangi, J. L. Prince and M. Sonka, The MICCAI Society book Series, Academic Press, New York, 2024, ch. 1, pp. 3–19.
16 X. Ning, S. Lee, Z. Wang, D. Kim, B. Stubblefield, E. Gilbert and N. Murthy, *Nat. Mater.*, 2011, **10**, 602–607.
17 X. Ning, W. Seo, S. Lee, K. Takemiya, M. Rafi, X. Feng, D. Weiss, X. Wang, L. Williams, V. M. Camp, M. Eugene, W. R. Taylor, M. Goodman and N. Murthy, *Angew. Chem.*, 2014, **53**, 14096–14101.
18 K. Takemiya, X. Ning, W. Seo, X. Wang, R. Mohammad, G. Joseph, J. S. Titterington, C. S. Kraft, J. A. Nye, N. Murthy, M. M. Goodman and W. R. Taylor, *JACC Cardiovasc. Imaging*, 2019, **12**(5), 875–886.
19 K. Takemiya, J. J. Roise, M. He, C. Taing, A. G. Rodriguez, N. Murthy, M. M. Goodman and W. R. Taylor, *PLoS One*, 2021, **16**, e0247673.
20 R. Dippel, T. Bergmiller, A. Bohm and W. Boos, *J. Bacteriol.*, 2005, **187**, 8332–8339.
21 R. Dippel and W. Boos, *J. Bacteriol.*, 2005, **187**, 8322–8331.
22 E. Bordignon, M. Grote and E. Schneider, *Mol. Microbiol.*, 2010, **77**, 1354–1366.
23 D. W. Abbott, M. A. Higgins, S. Hyrnuik, B. Pluvinage, A. Lammerts van Bueren and A. B. Boraston, *Mol. Microbiol.*, 2010, **77**, 183–199.
24 L. Clermont, A. Macha, L. M. Muller, S. M. Derya, P. von Zaluskowski, A. Eck, B. J. Eikmanns and G. M. Seibold, *J. Bacteriol.*, 2015, **197**, 1394–1407.
25 A. Axer, S. Hermann, G. Kehr, D. Clases, U. Karst, L. Fischer-Riepe, J. Roth, M. Fobker, M. Schafers, R. Gilmour and A. Faust, *ChemMedChem*, 2018, **13**, 241–250.
26 G. Gowrishankar, M. Namavari, E. B. Jouannot, A. Hoehne, R. Reeves, J. Hardy and S. S. Gambhir, *PLoS One*, 2014, **9**, e107951.
27 A. Zlitni, G. Gowrishankar, I. Steinberg, T. Haywood and S. Sam Gambhir, *Nat. Commun.*, 2020, **11**, 1250.
28 A. L. Bernstein, A. Dhanantwari, M. Jurcova, R. Cheheltani, P. C. Naha, T. Ivanc, E. Shefer and D. P. Cormode, *Sci. Rep.*, 2016, **6**, 26177.
29 M. L. James and S. S. Gambhir, *Physiol. Rev.*, 2012, **92**, 897–965.
30 M. W. Galper, M. T. Saung, V. Fuster, E. Roessl, A. Thran, R. Proksa, Z. A. Fayad and D. P. Cormode, *Investig. Radiol.*, 2012, **47**, 475–481.
31 G. Gowrishankar, J. Hardy, M. Wardak, M. Namavari, R. E. Reeves, E. Neofytou, A. Srinivasan, J. C. Wu, C. H. Contag and S. S. Gambhir, *J. Nucl. Med.*, 2017, **58**, 1679–1684.
32 T. Takeuchi, T. Kozu, S. Watanabe, M. Morita, K. Shiratori and I. Shibata, *Gastroenterol. Jpn.*, 1978, **13**, 395–400.
33 J. C. Murat, C. Castilla and H. Paris, *Comp. Biochem. Physiol. B*, 1978, **61**, 145–149.
34 P. Coma, L. Gomez-Chacon, B. Garcia-Serrano, E. Fernandez and M. A. Ortiz-Apodaca, *Clin. Chem.*, 1992, **38**, 223–226.
35 A. Compton, *Biochem. J.*, 1921, **15**, 681–686.
36 H. Bittencourt, M. H. Sleisenger and E. Weser, *Gastroenterology*, 1969, **57**, 410–414.
37 N. Jarkas, R. J. Voll and M. M. Goodman, *J. Labelled Compd. Radiopharm.*, 2013, **56**, 539–543.
38 J. Kihlberg, T. Frejd, K. Jansson, A. Sundin and G. Magnusson, *Carbohydr. Res.*, 1988, **176**, 271–286.
39 L. Greffe, M. T. Jensen, F. Chang-Pi-Hin, S. Fruchard, M. J. O'Donohue, B. Svensson and H. Driguez, *Chemistry*, 2002, **8**, 5447–5455.
40 M. Blanc-Muesser and H. D. Jacques Defaye, *Carbohydr. Res.*, 1978, **67**, 305–328.
41 H. Fujino, T. Fukuda, M. Nagatomo and M. Inoue, *J. Am. Chem. Soc.*, 2020, **142**, 13227–13234.
42 M. Blanc-Muesser and H. D. Jacques Defaye, *J. Chem. Soc. Perkin Trans. 1*, 1982, 15–18.
43 M. R. Sohail, D. Z. Uslan, A. H. Khan, P. A. Friedman, D. L. Hayes, W. R. Wilson, J. M. Steckelberg, S. Stoner and L. M. Baddour, *J. Am. Coll. Cardiol.*, 2007, **49**, 1851–1859.
44 S. K. Mulpuru, V. G. Pretorius and U. M. Birgersdotter-Green, *Circulation*, 2013, **128**, 1031–1038.
45 G. M. Viola, L. L. Awan and R. O. Darouiche, *Circulation*, 2010, **121**, 2085–2091.
46 B. Thorens and M. Mueckler, *Am. J. Physiol. Endocrinol. Metab.*, 2010, **298**, E141–E145.
47 L. Han, Q. Qu, D. Aydin, O. Panova, M. J. Robertson, Y. Xu, R. O. Dror, G. Skiniotis and L. Feng, *Nature*, 2022, **601**, 274–279.
48 D. Deng and N. Yan, *Protein Sci.*, 2016, **25**, 546–558.
49 G. D. Holman, *Biochem. J.*, 2018, **475**, 3511–3534.
50 D. Deng, P. Sun, C. Yan, M. Ke, X. Jiang, L. Xiong, W. Ren, K. Hirata, M. Yamamoto, S. Fan and N. Yan, *Nature*, 2015, **526**, 391–396.
51 H. Koepsell, *Pfluegers Arch.*, 2020, **472**, 1299–1343.
52 I. Vrhovac, D. Balen Eror, D. Klessen, C. Burger, D. Breljak, O. Kraus, N. Radovic, S. Jadrijevic, I. Aleksic, T. Walles, C. Sauvant, I. Sabolic and H. Koepsell, *Pfluegers Arch.*, 2015, **467**, 1881–1898.

53 I. Sabolic, I. Vrhovac, D. B. Eror, M. Gerasimova, M. Rose, D. Breljak, M. Ljubojevic, H. Brzica, A. Sebastiani, S. C. Thal, C. Sauvant, H. Kipp, V. Vallon and H. Koepsell, *Am. J. Physiol. Cell Physiol.*, 2012, **302**, C1174–C1188.
54 E. M. Wright, D. D. Loo and B. A. Hirayama, *Physiol. Rev.*, 2011, **91**, 733–794.
55 P. Song, A. Onishi, H. Koepsell and V. Vallon, *Expert Opin. Ther. Targets*, 2016, **20**, 1109–1125.
56 L. Ferte, A. Marino, S. Battault, L. Bultot, A. Van Steenbergen, A. Bol, J. Cumps, A. Ginion, H. Koepsell, L. Dumoutier, L. Hue, S. Horman, L. Bertrand and C. Beauloye, *Am. J. Physiol. Heart Circ. Physiol.*, 2021, **320**, H838–H853.
57 M. A. Hediger, E. Turk, A. M. Pajor and E. M. Wright, *Klin. Wochenschr.*, 1989, **67**, 843–846.
58 M. A. Hediger, E. Turk and E. M. Wright, *Proc. Natl. Acad. Sci. U. S. A.*, 1989, **86**, 5748–5752.
59 R. G. Wells, A. M. Pajor, Y. Kanai, E. Turk, E. M. Wright and M. A. Hediger, *Am. J. Physiol.*, 1992, **263**, F459–F465.
60 H. C. Chang, S. F. Yang, C. C. Huang, T. S. Lin, P. H. Liang, C. J. Lin and L. C. Hsu, *Mol. Biosyst.*, 2013, **9**, 2010–2020.
61 W. Boos and H. Shuman, *Microbiol. Mol. Biol. Rev.*, 1998, **62**, 204–229.
62 M. L. Oldham, D. Khare, F. A. Quiocho, A. L. Davidson and J. Chen, *Nature*, 2007, **450**, 515–521.
63 M. L. Oldham, S. Chen and J. Chen, *Proc. Natl. Acad. Sci. U. S. A.*, 2013, **110**, 18132–18137.
64 X. Duan, J. A. Hall, H. Nikaido and F. A. Quiocho, *J. Mol. Biol.*, 2001, **306**, 1115–1126.
65 F. A. Quiocho, J. C. Spurlino and L. E. Rodseth, *Structure*, 1997, **5**, 997–1015.
66 T. Ferenci, *Eur. J. Biochem.*, 1980, **108**, 631–636.
67 T. Ferenci, M. Muir, K. S. Lee and D. Maris, *Biochim. Biophys. Acta*, 1986, **860**, 44–50.
68 R. Benz, A. Schmid, T. Nakae and G. H. Vos-Scheperkeuter, *J. Bacteriol.*, 1986, **165**, 978–986.
69 A. Ranquin and P. Van Gelder, *Res. Microbiol.*, 2004, **155**, 611–616.
70 R. Benz, A. Schmid and G. H. Vos-Scheperkeuter, *J. Membr. Biol.*, 1987, **100**, 21–29.
71 C. Andersen, M. Jordy and R. Benz, *J. Gen. Physiol.*, 1995, **105**, 385–401.
72 E. Berkane, F. Orlik, A. Charbit, C. Danelon, D. Fournier, R. Benz and M. Winterhalter, *J. Nanobiotechnol.*, 2005, **3**, 3.
73 A. Charbit, *Front. Biosci.*, 2003, **8**, s265–s274.
74 K. Denker, F. Orlik, B. Schiffler and R. Benz, *J. Mol. Biol.*, 2005, **352**, 534–550.
75 R. Somavanshi, B. Ghosh and V. Sourjik, *PLoS Biol.*, 2016, **14**, e2000074.
76 C. Jardin, A. H. Horn, G. Schurer and H. Sticht, *J. Phys. Chem. B*, 2008, **112**, 13391–13400.
77 J. G. McCoy, E. J. Levin and M. Zhou, *Biochim. Biophys. Acta*, 2015, **1850**, 577–585.
78 J. G. McCoy, Z. Ren, V. Stanevich, J. Lee, S. Mitra, E. J. Levin, S. Poget, M. Quick, W. Im and M. Zhou, *Structure*, 2016, **24**, 956–964.
79 Z. Ren, J. Lee, M. M. Moosa, Y. Nian, L. Hu, Z. Xu, J. G. McCoy, A. C. M. Ferreon, W. Im and M. Zhou, *Proc. Natl. Acad. Sci. U. S. A.*, 2018, **115**, 5962–5967.
80 J. Thomson, Y. Liu, J. M. Sturtevant and F. A. Quiocho, *Biophys. Chem.*, 1998, **70**, 101–108.
81 K. Takemiya, S. Wang, Y. Liu, N. Murthy, M. M. Goodman and W. R. Taylor, *Biochem. Biophys. Res. Commun.*, 2024, **695**, 149467.
82 F. J. Alvarez, C. Orelle, Y. Huang, R. Bajaj, R. M. Everly, C. S. Klug and A. L. Davidson, *Mol. Microbiol.*, 2015, **98**, 878–894.
83 J. C. Spurlino, G. Y. Lu and F. A. Quiocho, *J. Biol. Chem.*, 1991, **266**, 5202–5219.
84 J. E. Fleming and H. Lynton, *Can. J. Chem.*, 1967, **45**, 353.
85 F. H. Allen, O. Kennard, D. G. Watson, L. Brammer, A. G. Orpen and R. Taylor, *J. Chem. Soc., Perkin Trans. 2*, 1987, S1–S19.
86 N. Sauvageot, A. Mokhtari, P. Joyet, A. Budin-Verneuil, V. S. Blancato, G. D. Repizo, C. Henry, A. Pikis, J. Thompson, C. Magni, A. Hartke and J. Deutscher, *J. Bacteriol.*, 2017, **199**(9), e00878.
87 Y. Le Breton, V. Pichereau, N. Sauvageot, Y. Auffray and A. Rince, *J. Appl. Microbiol.*, 2005, **98**, 806–813.
88 A. Mokhtari, V. S. Blancato, G. D. Repizo, C. Henry, A. Pikis, A. Bourand, M. de Fatima Alvarez, S. Immel, A. Mechakra-Maza, A. Hartke, J. Thompson, C. Magni and J. Deutscher, *Mol. Microbiol.*, 2013, **88**, 234–253.
89 P. Joyet, A. Mokhtari, E. Riboulet-Bisson, V. S. Blancato, M. Espariz, C. Magni, A. Hartke, J. Deutscher and N. Sauvageot, *Appl. Environ. Microbiol.*, 2017, **83**(13), e00038.
90 S. A. Shelburne III, H. Fang, N. Okorafor, P. Sumby, I. Sitkiewicz, D. Keith, P. Patel, C. Austin, E. A. Graviss, J. M. Musser and D. C. Chow, *J. Bacteriol.*, 2007, **189**, 2610–2617.
91 S. A. Shelburne III, D. B. Keith, M. T. Davenport, N. Horstmann, R. G. Brennan and J. M. Musser, *Mol. Microbiol.*, 2008, **69**, 436–452.
92 A. Rahmim, M. A. Lodge, N. A. Karakatsanis, V. Y. Panin, Y. Zhou, A. McMillan, S. Cho, H. Zaidi, M. E. Casey and R. L. Wahl, *Eur. J. Nucl. Med. Mol. Imag.*, 2019, **46**, 501–518.
93 G. Tomasi and L. Rosso, *Curr. Opin. Pharmacol.*, 2012, **12**, 569–575.
94 R. Kekuda, P. Saha and U. Sundaram, *Am. J. Physiol. Gastrointest. Liver Physiol.*, 2008, **294**, G1354–G1361.
95 Y. Li, K. M. Thelen, K. M. Fernandez, R. Nelli, M. Fardisi, M. Rajput, N. L. Trottier, G. A. Contreras and A. J. Moeser, *Am. J. Physiol. Gastrointest. Liver Physiol.*, 2022, **322**, G346–G359.
96 J. Park, I. S. Lee, K. H. Kim, Y. Kim, E. J. An and H. J. Jang, *Int. J. Mol. Sci.*, 2019, **20**(10), 2537.
97 P. Sharma, V. Khairnar, I. V. Madunic, Y. Singh, A. Pandyra, M. S. Salker, H. Koepsell, I. Sabolic, F. Lang, P. A. Lang and K. S. Lang, *Cell. Physiol. Biochem.*, 2017, **42**, 1358–1365.
98 M. Zhao, N. Li and H. Zhou, *Drug Des., Dev. Ther.*, 2023, **17**, 2011–2023.

99 P. L. Altman and K. Dittmer, *Dorothy., Blood and Other Body Fluids/Analysis and Compilation*, Federation of American Societies for Experimental Biology, Washington, 1961.
100 I. A. Hatton, E. D. Galbraith, N. S. C. Merleau, T. P. Miettinen, B. M. Smith and J. A. Shander, *Proc. Natl. Acad. Sci. U. S. A.*, 2023, **120**, e2303077120.
101 C. Scafoglio, B. A. Hirayama, V. Kepe, J. Liu, C. Ghezzi, N. Satyamurthy, N. A. Moatamed, J. Huang, H. Koepsell, J. R. Barrio and E. M. Wright, *Proc. Natl. Acad. Sci. U. S. A.*, 2015, **112**, E4111–E4119.
102 H. Koepsell, *Pharmacol. Ther.*, 2017, **170**, 148–165.
103 S. Tsunokake, E. Iwabuchi, Y. Miki, A. Kanai, Y. Onodera, H. Sasano, T. Ishida and T. Suzuki, *Breast Cancer Res. Treat.*, 2023, **201**, 499–513.
104 T. Inoue, M. Takemura, N. Fushimi, Y. Fujimori, T. Onozato, T. Kurooka, T. Asari, H. Takeda, M. Kobayashi, H. Nishibe and M. Isaji, *Eur. J. Pharmacol.*, 2017, **806**, 25–31.
105 H. Ohno, Y. Kojima, H. Harada, Y. Abe, T. Endo and M. Kobayashi, *Xenobiotica*, 2019, **49**, 463–473.
106 C. S. Hummel, C. Lu, J. Liu, C. Ghezzi, B. A. Hirayama, D. D. Loo, V. Kepe, J. R. Barrio and E. M. Wright, *Am. J. Physiol. Cell Physiol.*, 2012, **302**, C373–C382.
107 M. P. Lostao, B. A. Hirayama, D. D. Loo and E. M. Wright, *J. Membr. Biol.*, 1994, **142**, 161–170.
108 Y. Niu, R. Liu, C. Guan, Y. Zhang, Z. Chen, S. Hoerer, H. Nar and L. Chen, *Nature*, 2022, **601**, 280–284.
109 M. Namavari, G. Gowrishankar, A. Srinivasan, S. S. Gambhir, T. Haywood and C. Beinat, *J. Labelled Compd. Radiopharm.*, 2018, **61**, 408–414.
110 R. Boellaard, R. Delgado-Bolton, W. J. Oyen, F. Giammarile, K. Tatsch, W. Eschner, F. J. Verzijlbergen, S. F. Barrington, L. C. Pike, W. A. Weber, S. Stroobants, D. Delbeke, K. J. Donohoe, S. Holbrook, M. M. Graham, G. Testanera, O. S. Hoekstra, J. Zijlstra, E. Visser, C. J. Hoekstra, J. Pruim, A. Willemsen, B. Arends, J. Kotzerke, A. Bockisch, T. Beyer, A. Chiti, B. J. Krause and M. European Association of Nuclear, *Eur. J. Nucl. Med. Mol. Imag.*, 2015, **42**, 328–354.
111 K. Johnsrud, K. Skagen, T. Seierstad, M. Skjelland, D. Russell and M. E. Revheim, *J. Nucl. Cardiol.*, 2019, **26**, 883–893.
112 W. S. Lee, Y. Kanai, R. G. Wells and M. A. Hediger, *J. Biol. Chem.*, 1994, **269**, 12032–12039.
113 M. W. Song, W. Cui, C. G. Lee, R. Cui, Y. H. Son, Y. H. Kim, Y. Kim, H. J. Kim, S. E. Choi, Y. Kang, T. H. Kim, J. Y. Jeon and K. W. Lee, *Front. Pharmacol*, 2023, **14**, 1228646.
114 H. Y. Kueh, A. Champhekar, S. L. Nutt, M. B. Elowitz and E. V. Rothenberg, *Science*, 2013, **341**, 670–673.
115 S. Han, D. L. Hagan, J. R. Taylor, L. Xin, W. Meng, S. A. Biller, J. R. Wetterau, W. N. Washburn and J. M. Whaley, *Diabetes*, 2008, **57**, 1723–1729.
116 W. Meng, B. A. Ellsworth, A. A. Nirschl, P. J. McCann, M. Patel, R. N. Girotra, G. Wu, P. M. Sher, E. P. Morrison, S. A. Biller, R. Zahler, P. P. Deshpande, A. Pullockaran, D. L. Hagan, N. Morgan, J. R. Taylor, M. T. Obermeier, W. G. Humphreys, A. Khanna, L. Discenza, J. G. Robertson, A. Wang, S. Han, J. R. Wetterau, E. B. Janovitz, O. P. Flint, J. M. Whaley and W. N. Washburn, *J. Med. Chem.*, 2008, **51**, 1145–1149.
117 M. Obermeier, M. Yao, A. Khanna, B. Koplowitz, M. Zhu, W. Li, B. Komoroski, S. Kasichayanula, L. Discenza, W. Washburn, W. Meng, B. A. Ellsworth, J. M. Whaley and W. G. Humphreys, *Drug Metab. Dispos.*, 2010, **38**, 405–414.